



## RESEARCH ARTICLE

10.1002/2014JC010327

## Seasonal evolution of an ice-shelf influenced fast-ice regime, derived from an autonomous thermistor chain

M. Hoppmann<sup>1</sup>, M. Nicolaus<sup>1</sup>, P. A. Hunkeler<sup>1</sup>, P. Heil<sup>2,3</sup>, L.-K. Behrens<sup>1</sup>, G. König-Langlo<sup>1</sup>, and R. Gerdes<sup>1</sup><sup>1</sup>Alfred-Wegener-Institut Helmholtz-Zentrum für Polar-und Meeresforschung, Bremerhaven, Germany, <sup>2</sup>Australian Antarctic Division, Department of the Environment, Kingston, Tasmania, Australia, <sup>3</sup>Antarctic Climate and Ecosystems Cooperative Research Centre, University of Tasmania, Hobart, Tasmania, Australia

## Key Points:

- Ocean/ice-shelf interaction dominates coastal sea-ice mass balance
- Basal energy balance reveals platelet layer ice-volume fraction of a fifth
- Thermistor chain heating is a suitable tool to study platelet-layer evolution

## Correspondence to:

M. Hoppmann,  
Mario.Hoppmann@awi.de

## Citation:

Hoppmann, M., M. Nicolaus, P. A. Hunkeler, P. Heil, L.-K. Behrens, G. König-Langlo, and R. Gerdes (2015), Seasonal evolution of an ice-shelf influenced fast-ice regime, derived from an autonomous thermistor chain, *J. Geophys. Res. Oceans*, 120, 1703–1724, doi:10.1002/2014JC010327.

Received 18 JUL 2014

Accepted 30 JAN 2015

Accepted article online 6 FEB 2015

Published online 19 MAR 2015

**Abstract** Ice shelves strongly interact with coastal Antarctic sea ice and the associated ecosystem by creating conditions favorable to the formation of a sub-ice platelet layer. The close investigation of this phenomenon and its seasonal evolution remains a challenge due to logistical constraints and a lack of suitable methodology. In this study, we characterize the seasonal cycle of Antarctic fast ice adjacent to the Ekström Ice Shelf in the eastern Weddell Sea. We used a thermistor chain with the additional ability to record the temperature response induced by cyclic heating of resistors embedded in the chain. Vertical sea-ice temperature and heating profiles obtained daily between November 2012 and February 2014 were analyzed to determine sea-ice and snow evolution, and to calculate the basal energy budget. The residual heat flux translated into an ice-volume fraction in the platelet layer of  $0.18 \pm 0.09$ , which we reproduced by an independent model simulation and agrees with earlier results. Manual drillings revealed an average annual platelet-layer thickness increase of at least 4 m, and an annual maximum thickness of 10 m beneath second-year sea ice. The oceanic contribution dominated the total sea-ice production during the study, effectively accounting for up to 70% of second-year sea-ice growth. In summer, an oceanic heat flux of  $21 \text{ W m}^{-2}$  led to a partial thinning of the platelet layer. Our results further show that the active heating method, in contrast to the acoustic sounding approach, is well suited to derive the fast-ice mass balance in regions influenced by ocean/ice-shelf interaction, as it allows subdiurnal monitoring of the platelet-layer thickness.

## 1. Introduction

Sea ice is a critical component in the global climate system, and an important marine habitat. Its influence ranges from the formation of polar deep water masses involved in the global thermohaline circulation [Fahrbach *et al.*, 2001], over the global radiation budget via albedo effects on the lower atmosphere [Perovich *et al.*, 2007] to the heat and light distribution in the water column [Nicolaus *et al.*, 2012]. In the Southern Ocean, sea ice spreads over millions of square kilometers at all times of the year. The Antarctic sea-ice cover has, on average, expanded since the late 1970s [Parkinson and Cavalieri, 2012], an evolution which is the sum of large regional differences whose drivers are currently only poorly understood. Proposed explanations include teleconnections of atmospheric circulation systems and changes in wind forcing [Liu *et al.*, 2004; Lefebvre and Goosse, 2008; Simpkins *et al.*, 2012; Holland and Kwok, 2012; Li *et al.*, 2014], increased precipitation [Fichefet and Maqueda, 1999; Liu and Curry, 2010], as well as atmosphere and ocean feedbacks [Zhang, 2007; Stammerjohn *et al.*, 2008]. Several other studies investigated the influence of an increased freshwater flux by enhanced melting of Antarctic ice shelves on sea-ice formation, but results remain inconclusive [Swingedouw *et al.*, 2008; Bintanja *et al.*, 2013, 2015; Swart and Fyfe, 2013]. In order to understand the complex interactions, much more insight into the relevant processes is needed.

The changing large-scale wind patterns almost exclusively affect the drifting pack ice, while sea ice attached to coastal features is often strongly influenced by nearby ice shelves [e.g., Mahoney *et al.*, 2011; Smith *et al.*, 2012]. This land-fast sea ice (fast ice) is an important interface between the Antarctic ice sheet and the pack ice or the ocean [Massom *et al.*, 2001] and constitutes between 5% and 35% of total sea-ice area during months of maximum and minimum total sea-ice area in East Antarctica [Fraser *et al.*, 2012], respectively. It is ideal to study in detail the processes which modify Antarctic sea-ice properties in general [Heil *et al.*, 2011].

This is an open access article under the terms of the Creative Commons Attribution-NonCommercial-NoDerivs License, which permits use and distribution in any medium, provided the original work is properly cited, the use is non-commercial and no modifications or adaptations are made.

Research on the physical properties of fast ice has largely been focusing on areas close to Antarctic bases, for example, at Lützow Holm Bay [Kawamura *et al.*, 1997; Ohshima *et al.*, 2000; Uto *et al.*, 2006], Prydz Bay [Heil, 2006; Tang *et al.*, 2007; Lei *et al.*, 2010], and McMurdo Sound [Jeffries *et al.*, 1993; Purdie *et al.*, 2006; Gough *et al.*, 2012].

Some of these locations exhibit characteristics that reflect a strong ocean/ice-shelf interaction, manifested through the presence of a sub-ice platelet layer. This special sea-ice type not only modifies the properties, mass and energy balance of an overlying solid sea-ice cover [Hoppmann *et al.*, 2015], it also acts as a habitat for a substantial amount of algal biomass [Arrigo *et al.*, 1993; Günther and Dieckmann, 1999, 2001], provides a protective environment for coastal fish species [Vacchi *et al.*, 2000], and might also allow conclusions about processes in the ice-shelf cavity. While the formation mechanisms of ice crystals in supercooled waters are in principle understood [Mager *et al.*, 2013], little is known about the spatiotemporal variability of sub-ice platelet layers in Antarctica. Despite their importance for the climate and ecosystem, a means to effectively monitor Antarctic platelet layers remains a challenge due to the lack of suitable methodology. A promising approach to determine its spatial variability is the application of (ground-based) multi-frequency EM induction sounding [Hunkeler *et al.*, 2015]. However, no method is currently available to provide information about its temporal evolution without the need for extensive logistics.

Providing a relatively inexpensive alternative to field campaigns, autonomous Ice Mass Balance Buoys (IMBs) have been widely used in recent years to monitor the sea-ice mass balance at a fixed study site [Perovich and Elder, 2001]. Typical IMBs are equipped with a thermistor chain extending through the snow and sea-ice cover into the upper ocean, as well as with acoustic sensors monitoring the position of the ice/water and air/snow (air/ice) interfaces [Richter-Menge *et al.*, 2006]. They usually also record GPS position, sea level pressure and 2 m air temperature. If combined, these data not only reveal changes in the sea-ice mass balance due to ice growth, surface melt, and bottom ablation, they also provide valuable information about the snow cover. In a next step, the observed changes can be correlated with variables associated with the external drivers, such as the beginning and duration of the summer melt season, the length of the growth season, and the oceanic heat flux. By doing so, one is not only able to obtain information about the state of the sea-ice cover, but also to gain important insight into the driving forces behind the ongoing changes. However, these instruments are usually expensive and take a substantial effort to deploy.

Recently, a promising new type of thermistor chain IMB has been developed [Jackson *et al.*, 2013], which is significantly lower in cost than comparable instruments and very easy to deploy. A special feature of this design is the ability to actively heat embedded resistors near the temperature sensors, which is described in more detail below. Despite the growing demand and application of this buoy type, no consistent data set has been published to date and the instrument's full potential is still to be determined.

In this study, we analyzed data from such a thermistor chain, in order to determine the physical properties of an ice-shelf influenced sea-ice cover and its seasonal evolution. The instrument was operated on the fast ice of Atka Bay, eastern Weddell Sea, between November 2012 and February 2014. These measurements were combined with continuous meteorological and oceanographic data, as well as manual thickness measurements and model simulations, in order to quantify the processes governing sea-ice mass balance, and to characterize their seasonality. At the same time, we assessed the potential of this relatively new instrument design on the basis of this unique data set, highlighting its advantages and pointing out its caveats to assist the interpretation of such data sets in future studies.

## 2. Methods

### 2.1. Field Setting

This study was conducted on the generally first-year fast ice of Atka Bay, a sheltered embayment adjacent to the Ekström Ice Shelf (Figure 1). The geographic setting is described in more detail in Hoppmann *et al.* [2015] and references therein. A large iceberg (B15G) grounded in front of Atka Bay in September 2012 (Figure 1b, dashed red curve), which sheltered the fast ice and prevented a breakup in early 2013. The fast ice survived the summer and became thick second-year sea ice in 2013. The iceberg dislodged itself in August 2013 and drifted away westward with the coastal current. Between 9 and 16 February 2014, approximately two-thirds of the fast-ice area finally disintegrated into small floes, marking the end of our study (Figure 1c).

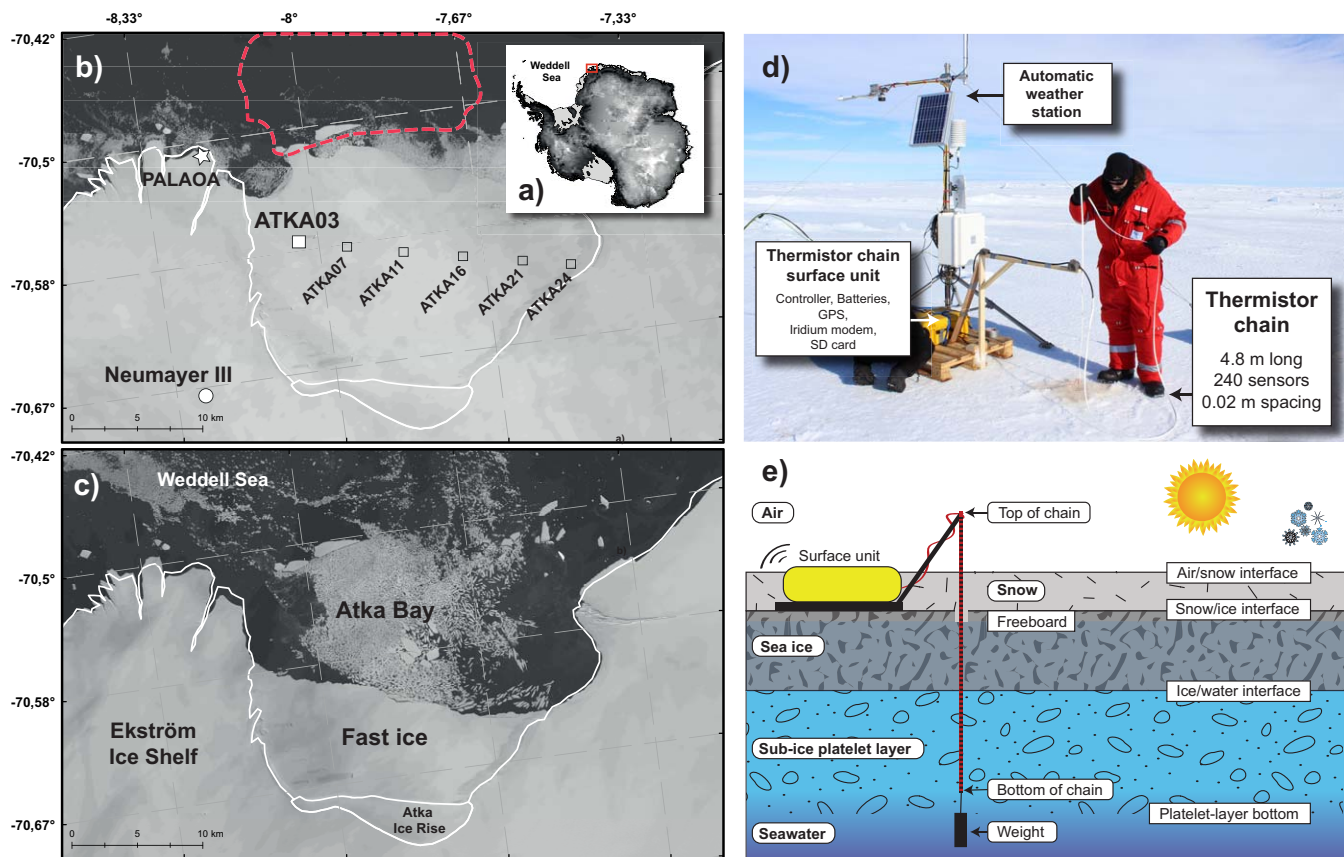


**Figure 1.** Study area and thermistor chain deployment. (a) Location of this study on a map of Antarctica. (b) Landsat image of Atka Bay at the beginning of the fast-ice breakup (9 February 2014). The main sampling site was located 3 km east of the western ice-shelf edge (ATKA03, white square). Auxiliary study sites are also indicated (squares), along with the former position of grounded iceberg B15G (dashed red curve). (c) Landsat image from 16 February 2014, when 2/3 of the sea ice has broken up. Landsat imagery courtesy of NASA Goddard Space Flight Center and U.S. Geological Survey, coastline data from Antarctic Digital Database 6.0. (d) Photo of thermistor chain deployment (21 November 2012). (e) Schematic diagram of thermistor chain extending through air, snow, sea ice, and the sub-ice platelet layer.

## 2.2. Thermistor Chains

On 21 November 2012, we deployed a thermistor chain (Scottish Association for Marine Science, Oban, Scotland) approximately 3 km from the Ekström Ice Shelf (Figure 1b). This location is a regular site of an ongoing sea-ice monitoring program, mainly chosen for logistical reasons. It was within an area of moderately deformed sea ice, which initially formed in March/April 2012. For consistency with other studies [Hoppmann *et al.*, 2015; Paul *et al.*, 2015; Hunkeler *et al.*, 2015], we refer to this site as ATKA03.

The vertical thermistor chain (TC) was installed on level sea ice, through a 0.05 m diameter borehole (Figure 1d). It consisted of 240 thermistors at a spacing of 0.02 m, with a total length of 4.8 m. To prevent the chain from floating upward in the platelet layer, we attached a weight of 3 kg to the end of the chain. The hole did not refreeze all the way up to the original snow/ice interface due to the large positive freeboard, so it was filled up with snow after deployment. For our analysis we neglect this effect, and define the original snow/ice interface as our reference snow/ice interface.

The surface unit was placed onto a wooden rack for stability, with a side arm to guide the chain (Figure 1e). The temperature sensors (Maxim DS28EA00) have a resolution of 0.0625°C, and a worst-case accuracy of ±2°C [Jackson *et al.*, 2013]. We did not calibrate the chain, as the temperature sensors are offset-corrected by the manufacturer in a precision temperature-controlled water bath at 1°C. Sensor drift is considered low. The unique feature of this design is the operation similar to a combination of constant-current hot-wire anemometer and needle-probe thermal conductivity mode: after each regular temperature reading, embedded resistors (1 kΩ) near the temperature sensors are heated to above ambient temperature with an excitation voltage of 8 V, generating 63 mW of thermal energy. Heat is conducted away from the thermistors at a rate dependent on the

temperature gradient, the thermal conductivity of the surrounding medium and its flow rate, if liquid. Needle-probe thermal conductivity measurements were previously in snow research [Sturm and Johnson, 1992; Riche and Schneebeli, 2013], while hot-wire anemometry is a standard technique of experimental fluid dynamics and has been described, for example, by La Barbara and Vogel [1976] and Perry [1982]. Generally, a greater temperature rise is expected in air and snow than in water and ice due to their lower thermal conductivities. Since ice and water thermal conductivities lie very close together, the additional cooling introduced by a nonzero flow velocity in water may counteract the seawater's slightly lower thermal conductivity, potentially leading to difficulties in the determination of an ice/water interface. A quantitative relationship between the temperature response of this instrument and the thermal conductivity or flow speed of a medium has not been found yet, mostly due to the complex geometry, and this is also beyond the scope of this study. However, we will investigate in detail how well the instrument is suited to accurately determine the location of the interfaces between air, snow, ice, and water under field conditions. A full description of the TC and the "heating mode" is available in Jackson *et al.* [2013].

In our study, the heating duration and duty cycle were 120 s and 100% (of 63 mW), respectively, while the temperature rise was recorded after 30 s and 120 s. This configuration represents the default setting, recommended by Jackson *et al.* [2013] to provide a clear separation between the different media without reaching saturation. The temperature difference after 30 s of heating is referred to as "30 s heating" or  $\delta T_{30}$  throughout this paper. The temperature difference after 120 s of heating is referred to as "120 s heating" or  $\delta T_{120}$ , accordingly.

Upon deployment, snow depth, freeboard, and sea-ice thickness at ATKA03 were 0.01 m,  $0.40 \pm 0.05$  m, and  $2.45 \pm 0.05$  m, respectively. Determination of freeboard was difficult due to ice platelets clogging the borehole. The high initial thickness was the result of early formation and additional thickening due to floe-raftering. Sub-ice platelet-layer thickness was 4 m, with several interfaces of varying mechanical resistance within the layer. Due to its deployment late in the growth season, the chain did not extend below the platelet layer. In the first 3 weeks, the TC was configured to record the data every 6 h. It was reconfigured to hourly measurements on 11 December 2012. During February 2013, the sea ice became nearly isothermal. To save energy, the measurement interval was set to twice a day from February 2013. The batteries were changed on 28 April 2013 and again on 5 January 2014, to prepare for a potential sea-ice breakup and subsequent drift into the central Weddell Sea. However, the instrument ceased operation during sea-ice disintegration on 9 February 2014 (Figure 1b).

Due to the variable measurement intervals, the data were interpolated to a daily grid. The thermistor numbers were converted to depth, with the original snow/ice interface as the zero reference. Data from one broken sensor were removed. Erroneous thermistor readings, appearing as spikes in the temperature profiles, occurred sporadically (about 200 instances), and were removed manually. Spikes in the heating data were removed automatically, and the missing data points were linearly interpolated. Air/snow/ice interfaces were extracted automatically from temperature and heating profiles. The algorithms are not supplied because they were specifically tuned to this data set. The ice/water interface was determined by visual inspection to ensure the highest possible quality.

The temperature profiles and the interfaces extracted from heating profiles were used to calculate the sea-ice basal energy balance. Sea-ice growth, which is essentially a phase change at the ice bottom (latent heat flux,  $F_l$ ), is a function of the conductive heat transfer through the sea ice to the air ( $F_c$ ), the specific heat flux due to internal warming or cooling ( $F_s$ ), and the oceanic heat flux ( $F_w$ ). Following the approach of Gough *et al.* [2012], we calculated the oceanic heat flux  $F_w$  by a residual method [McPhee and Untersteiner, 1982; Purdie *et al.*, 2006] as

$$F_w = F_c + F_l + F_s. \tag{1}$$

We calculated the conductive, latent, and sensible heat fluxes after Semtner [1976]:

$$F_c = k_{si} \cdot \frac{\partial T}{\partial z}, \tag{2}$$

$$F_l = \rho_{si} \cdot L_f \cdot \frac{\partial H}{\partial t}, \tag{3}$$

$$F_s = -\rho_{si} \cdot c_{si} \cdot \frac{\partial T}{\partial t} \cdot \Delta H, \quad (4)$$

where the thermal conductivity  $k_{si}(\rho, S, T)$  is given by *Pringle et al.* [2007],  $\frac{\partial T}{\partial z}$  is the sea-ice temperature gradient,  $z$  is the vertical coordinate,  $\rho_{si}$  is sea-ice density,  $L_f(S, T)$  is the sea-ice latent heat of fusion given by *Yen* [1981] with a typographical error corrected as described by *Pringle et al.* [2007],  $\frac{\partial H}{\partial t}$  is the sea-ice growth rate,  $c_{si}(S, T)$  is the specific heat capacity [*Yen*, 1981],  $\frac{\partial T}{\partial t}$  is the temporal gradient in sea-ice temperature, and  $H$  is the position of the ice/water interface. The latent heat  $L_f(S, T)$  and the specific heat of sea ice  $c_{si}(S, T)$  are functions of its temperature and salinity according to *Untersteiner* [1961] and *Yen et al.* [1991]. Upward heat fluxes, warming and melting have positive sign, and  $z$  decreases from zero at the sea-ice surface. The energy balance has to be solved for a near-bottom reference level  $z_r$ , through which heat transport by brine convection is unlikely to contribute significantly [*Gough et al.*, 2012]. A stable bulk salinity may provide the necessary indication for this [*Petrich et al.*, 2006]. The selection of the reference level is critical for the calculation of  $F_c$  due to the nonlinearity of the vertical sea-ice temperature profile. A variety of reference levels have been used in the literature, most recently summarized by *Lei et al.* [2014]. *Gough et al.* [2012] defined the reference layer at 0.15 m above the ice/water interface, in a study comparable to ours. Based on the latter study and in agreement with our salinity measurements from the sea-ice core near ATKA03 (Figure 3), we used a reference level of 0.16 m from the ice/water interface for which we calculated the energy balance. The position of the ice/water interface  $H$  and also its change with time  $\frac{\partial H}{\partial t}$  were derived from the heating profiles with an uncertainty of  $\pm 0.02$  m. The reference level always followed the ice/water interface by  $z_r = H + 0.16$  m. The temperature gradient  $\frac{\partial T}{\partial z}$  across the reference level is obtained by a linear fit to all thermistors within  $\pm 0.14$  m of  $z_r$ .  $\frac{\partial T}{\partial t}$  is determined from the temperature  $T$  at the same level in neighboring time steps. Salinity is taken near  $z_r$  from the interpolated profile in Figure 3. We assumed  $\rho_{si}$  is  $910 \text{ kg m}^{-3}$  throughout, which is near the top of the range for multiyear sea ice reviewed by *Timco and Frederking* [1996]. This is slightly higher than the density measured from a sea-ice core in December 2012, where brine loss occurred during the measurement. The sea-ice growth rate was calculated as the temporal change in the evolution of the ice/water interface, derived from the  $\delta T_{120}$  data. The interface had previously been smoothed to remove the discrete steps originating from the thermistor spacing.

In order to assess the instrument's ability to detect the presence of a sub-ice platelet layer, we compared our main data set to a similar one obtained by a thermistor chain of the same type, deployed in the Weddell Sea during Polarstern cruise ANT-XXIX/9. This IMB was installed on a platelet-free floe at  $74^\circ 23.340' \text{ S}$ ,  $33^\circ 24.012' \text{ W}$  on 5 February 2014.

### 2.3. Automatic Weather Station

We twice deployed an automatic weather station (AWS) at ATKA03. First, it was operated from 2 October to 27 December 2012, but only data since the deployment of the TC (21 November 2012) are shown here. The AWS was recovered to avoid instrument loss due to a weakening of the fast-ice cover in late summer. Second, we deployed the same setup again a few meters from the thermistor chain on 31 May 2013. Measurements comprised air temperature and relative humidity (shielded HMP155A, Vaisala), barometric pressure (61302V, RM Young Company), wind speed and direction (Marine Wind Monitor 05106-5, RM Young Company) as well as downward and upward longwave and shortwave radiation (CNR4, Kipp and Zonen) in 2 m height at 1 min intervals. We also recorded snow height using an acoustic sounder (SR50A, Campbell Scientific) as an independent measurement to compare to snow depth derived from TC temperature and heating profiles. Finally, the AWS data were combined with data obtained at the meteorological observatory of Neumayer III [*König-Langlo and Loose*, 2007] to generate a consistent forcing for a thermodynamic sea-ice growth model [*Bitz and Lipscomb*, 1999; *Hoppmann et al.*, 2015].

### 2.4. Oceanographic Data

We used oceanographic data from the Perennial Acoustic Observatory in the Antarctic Ocean (PALAOA) [*Boebel et al.*, 2006]. An unpumped Sea-Bird Electronics (SBE) 37 MicroCAT was installed in the water column at a depth of about 155 m, 70 m below the ice shelf bottom and 90 m above the sea floor, in 2006. Since then, PALAOA was gradually transported closer to the ice-shelf edge due to the flowing glacier, and an end of its operation is expected in 2015. The instrument continuously records conductivity, temperature, and pressure at 30 min intervals, with an accuracy of  $\pm 0.0003 \text{ S m}^{-1}$ ,  $\pm 0.002^\circ \text{ C}$ , and  $\pm 0.5$  m, respectively.

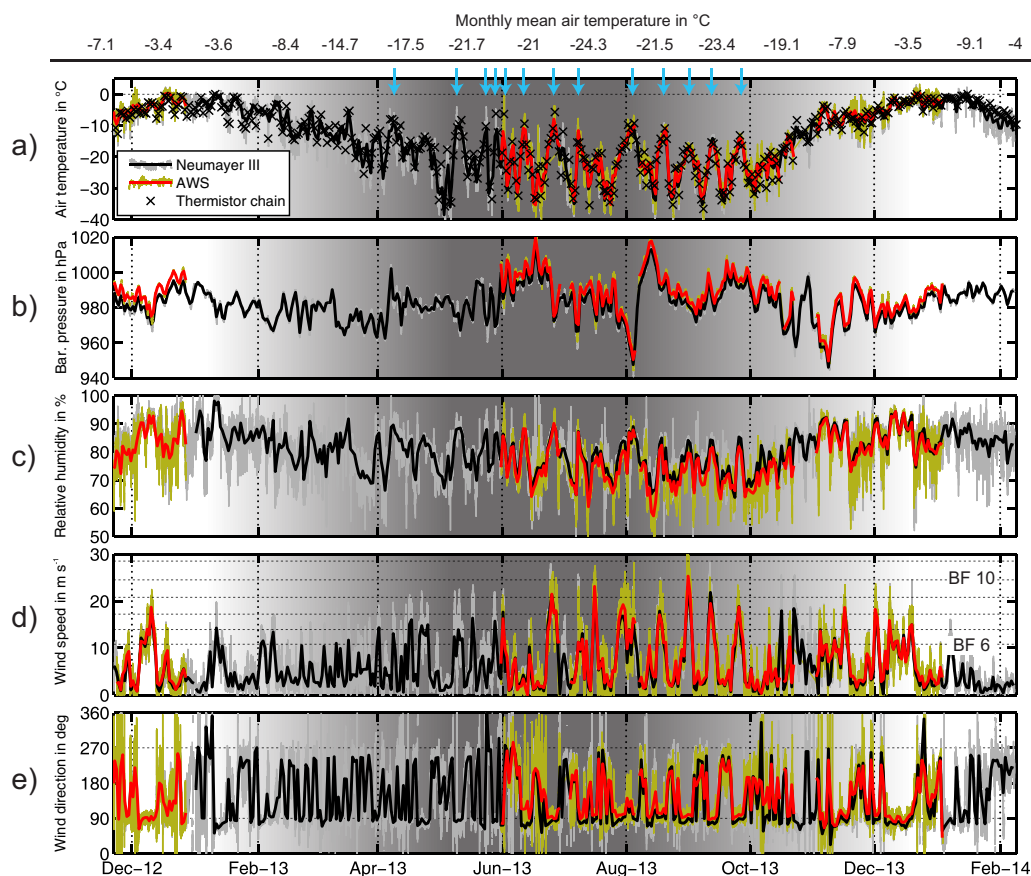


**Figure 2.** Meteorological conditions during the study period, as measured by the automatic weather station (red/green) and at Neumayer III (black/gray). Thin curves represent the measurements every minute, thick curves are daily averages. (a) Air temperature (2 m); (b) barometric pressure; (c) relative humidity; (d) wind speed (BF: Beaufort) and (e) wind direction. The blue arrows indicate the passage of synoptic systems in winter, associated with an advection of warm air, lower barometric pressure, high relative humidity, and strong easterly winds. The shaded area illustrates the annual cycle of polar day and night.

The distance to ATKA03 was  $\sim 10$  km in 2012/2013 (Figure 1b). The data set was checked for consistency and it can safely be assumed that the recordings were not affected by ice accretion on the instrument due to the presence of supercooled water. From the measurements, we calculated absolute salinity, potential temperature, and the surface freezing point using the Gibbs Seawater (GSW) Oceanographic Toolbox [McDougall and Barker, 2011].

### 2.5. Sea-Ice Cores

Two full-thickness, 0.09 m diameter cores to determine sea-ice physical properties were retrieved at ATKA03 on 19 and 27 December 2013. We measured in situ temperatures in the core from 19 December in 0.1 m intervals, using a hand-held thermometer inserted into 2 mm holes drilled to the center of the core. The core was packed in a styrofoam box, temporarily stored at Neumayer III, and later transported to Bremerhaven at  $-20^{\circ}\text{C}$  in order to perform a texture analysis. We drilled another core on 27 December, which was segmented into 0.1 m pieces on a bench immediately after being brought to the surface. The porosity of the segments was high and brine drainage could not be prevented. The segments were sealed in plastic boxes and transported to the laboratory. The density of each segment was calculated using a mass/volume approach [Timco and Frederking, 1996]. The segments were melted at a temperature of  $4^{\circ}\text{C}$  to minimize cell damage to algae present in the sea ice. Salinity was determined using a calibrated conductivity meter (WTW Cond3110). The samples were filtered and Chlorophyll-a was measured by a fluorometric method [Welschmeyer, 1994]. We used the sea-ice temperature, salinity, and density profiles to calculate brine and gas volume fractions according to Leppäranta and Manninen [1988]. Horizontal and vertical thin sections of the archived core were prepared and photographed between crossed polarizers.

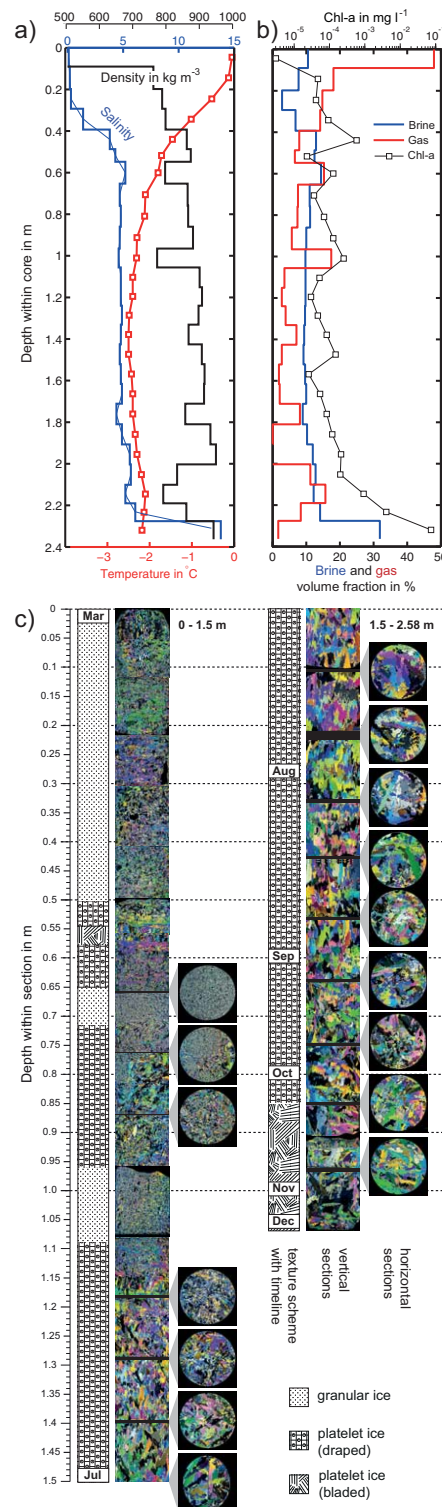


**Figure 3.** Sea-ice properties from cores retrieved at ATKA03 in December 2012. (a) Temperature (red), salinity (blue), and density profiles (black). The thin blue curve represents an interpolated salinity profile. (b) Brine (blue) and gas volume fractions (red), and Chlorophyll-a content (black). (c) Horizontal and vertical thin sections, photographed between crossed polarizers. The texture scheme to the left of the respective vertical thin sections was derived by visual inspection. The formation time in 2012 was determined by comparison to sea-ice thickness measurements (see text).

### 2.6. Drillings

Since the 4.8 m long thermistor chain did not extend through the entire platelet layer, the temperature and heating data shown here do not allow unambiguous conclusions about the evolution of its thickness. In order to reveal the platelet-layer's spatiotemporal evolution across the entire Atka Bay, we provide additional platelet-layer thickness data obtained by manual drillings at different sites throughout the study. One measurement was performed per site and visit. We thereby expand the study of Hoppmann *et al.* [2015], who described the platelet-layer evolution under first-year fast ice, to second-year fast ice.

### 2.7. Sea-Ice Growth Simulation

We simulated fast-ice growth by a one-dimensional, thermodynamic model [Bitz and Lipscomb, 1999] forced with local atmospheric data, and with snow depth derived from TC temperature profiles. We modified the original sea-ice growth rate  $\frac{\partial H}{\partial t}$  in the model by

$$\frac{\partial H}{\partial t}(\beta) = \frac{1}{1-\beta} \cdot \frac{\partial H}{\partial t}, \quad (5)$$

where  $\beta$  is the fraction of solid ice mass in a defined volume in the platelet layer (ice-volume fraction).

The initial setup and preparation of the forcing data were performed as described by Hoppmann *et al.* [2015], with corrections applied to air temperature (+0.5°C), relative humidity (-2%), barometric pressure (+4.1 hPa), and upward longwave radiation (+6.5 W m<sup>-2</sup>) to account for the different meteorological conditions on the sea ice compared to Neumayer III on the ice shelf (see Figure 2).

## 3. Results

This section is structured as follows: first, we highlight the environmental conditions during the study period, then we present results from our sea-ice core analysis. We investigate our main data set, thermistor chain temperature and heating profiles, and use these to calculate the basal energy balance. We then determine sea-ice growth from conductive heat flux alone and compare our observations to simulated fast-ice growth. Finally, we complement the results of our main data set with results of manual sub-ice platelet-layer thickness measurements and oceanographic conditions.

### 3.1. Environmental Conditions

Between TC deployment and mid-December 2012, the 2 m air temperature remained below the freezing point (Figure 2a). On 17 December, daily average temperatures rose above the freezing point for four consecutive days, before steadily decreasing until April 2013. During late autumn and winter, the air temperature fluctuated widely. Sudden changes in daily average air temperatures in excess of 20 K were recorded over 2 or 3 days. The overall minimum daily mean temperature of  $-38.5^{\circ}\text{C}$  was measured on 3 May 2013. Temperatures stabilized in early spring, and increased again from October 2013.

Storm activities, accompanied by increased wind speed and warm air advection, occurred about twice a month during the entire study, and about once per week during winter (Figure 2d). Those events were always associated with easterly winds (Figure 2e). These observations are in accordance with the general climatology of Neumayer III [König-Langlo *et al.*, 1998].

### 3.2. Sea-Ice Cores

The sea-ice core recovered at ATKA03 on 19 December 2012 was 2.58 m long. There was no snow, freeboard was about 0.4 m, and the platelet-layer thickness was about 4 m. The core obtained on 27 December 2012 was 2.4 m long, without any snow on top. The platelet-layer thickness was 4.2 m, and freeboard was not recorded.

Temperatures were near-isothermal below 0.65 m, and above  $-2.5^{\circ}\text{C}$  throughout the entire sea-ice core (Figure 3a). Salinity ranged from 0 at the surface to 13.8 in the skeletal layer at the bottom, with an overall average of 4.54. Sea-ice density was on average  $850\text{ kg m}^{-3}$ , with a minimum of  $490\text{ kg m}^{-3}$  near the top. This measurement underestimated the real density by up to 10% due to imprecise sawing, missing ice pieces, and especially brine loss at these high temperatures. For our calculation of air-volume fraction, we therefore used a sea-ice density of  $910\text{ kg m}^{-3}$ . Air volume fraction was on average 9%, and highest at the top of the core ( $>40\%$ ), which is explained by surface melt and brine drainage. The brine volume fraction was on average 11%, with the usually observed maximum in the skeletal layer of 35%.

The crystal structure (Figure 3c) was classified by visual inspection of thin sections from the sea-ice core, acknowledging that this interpretation may be subjective. Fine-grained crystals and air inclusions were evident in the upper 0.5 m of the core. While crystal edges in the upper layer had largely eroded, these crystals mostly resembled typical granular new ice formed under turbulent conditions. In the next 0.15 m, the texture showed distinct, albeit randomly oriented frazil crystals. We refer to this texture as platelet ice [Eicken and Lange, 1989; Jeffries *et al.*, 1993; Tison *et al.*, 2013; Dempsey *et al.*, 2010], with a crystal structure unlike that of granular or columnar ice [Dempsey *et al.*, 2010]. Multiple rafting was indicated by fine-grained crystals, typical of snow ice (0.66–0.71 m), followed by platelet ice, and again by granular ice near 1 m. Below 1.15 m, larger crystals of draped platelet ice [Tison *et al.*, 2013; Dempsey *et al.*, 2010], also sometimes referred to as mixed columnar/platelet ice [Mahoney *et al.*, 2011] were apparent throughout a large part of the core length. Below 2.35 m, the shape of the platelets became blade-like [Eicken and Lange, 1989; Tison *et al.*, 2013; Dempsey *et al.*, 2010]. The growth history of the sea ice was determined by comparison to thickness measurements made at ATKA03 throughout 2012 [Hoppmann *et al.*, 2015]. These measurements started in mid-June, when the sea ice was already about 1.4 m thick. Rafting seemed to have occurred until May. Continuous thermodynamic growth set in afterward (at approximately 1.15 m), and was immediately disrupted by the presence of platelets. In summary, about 25% of the core consisted of granular ice (and eventually snow ice), the other 75% of platelet ice. A pure columnar texture was not observed.

### 3.3. Temperature and Heating Profiles

Figure 4 presents the main data set of this study, comprising (a) temperature, (b)  $\delta T_{30}$ , and (c)  $\delta T_{120}$  measurements obtained by the TC between 21 November 2012 and 9 February 2014, interpolated to daily profiles. The prominent vertical structures in Figures 4b and 4c were a result of a drop in voltage applied to the resistors during heating.

In the following, we will try to uncover the variety of information hidden in these data: the temporal evolution of (1) the snow cover, (2) the snow/ice interface (including surface melt); (3) the ice/water interface (sea-ice growth); (4) the presence of internal melt and refreezing; (5) sub-ice platelet-layer thickness; (6) conductive heat flux; and finally (7) the basal energy balance including the calculation of a residual (oceanic) heat flux. The effect of solar radiation penetrating into the snow and potentially leading to a warming of the upper thermistors is neglected throughout this paper.

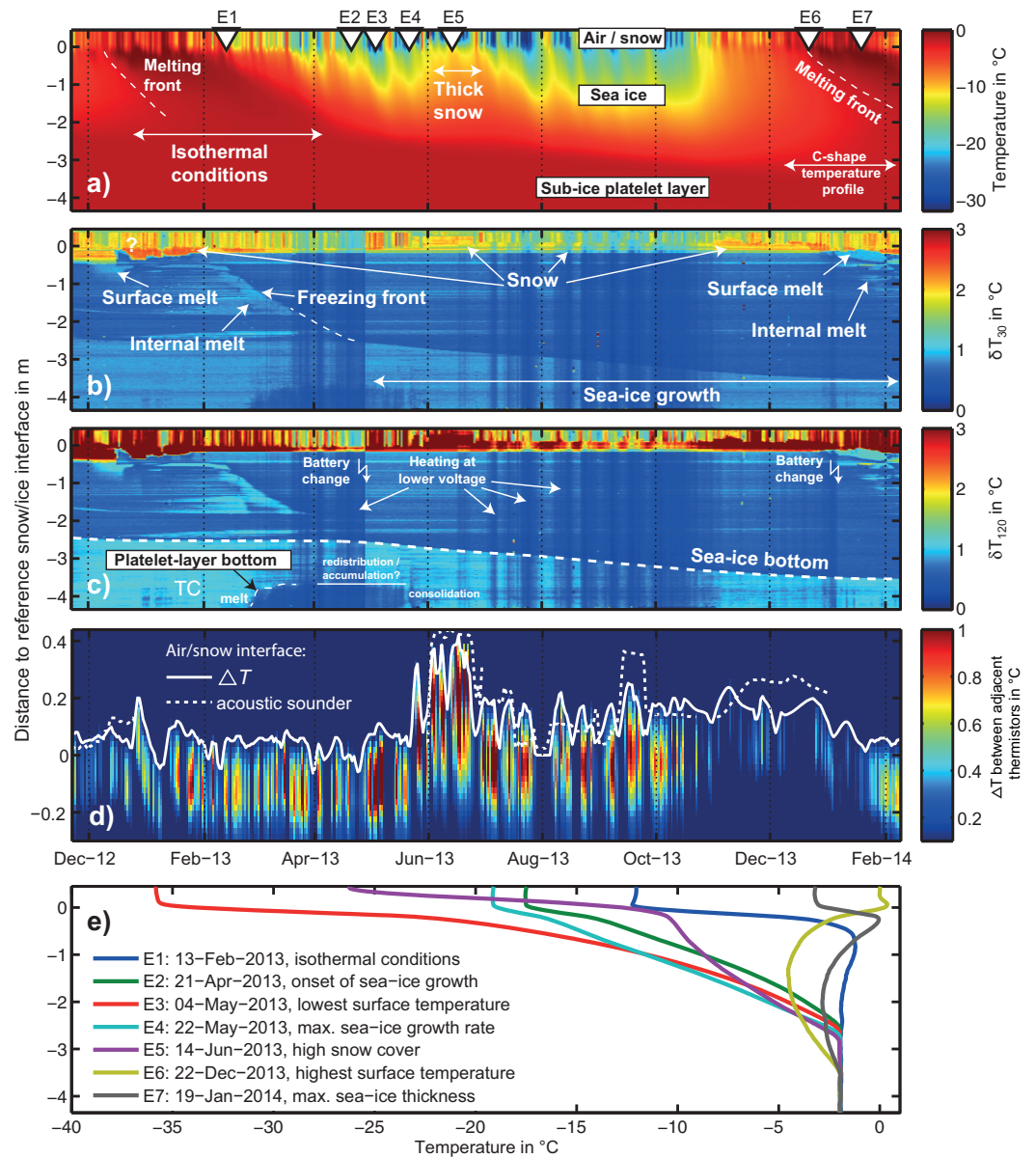


**Figure 4.** Data measured by the thermistor chain during the study period. (a) Daily temperature profiles; (b) temperature rise after 30 s heating ( $\delta T_{30}$ ); (c) temperature rise after 120 s heating ( $\delta T_{120}$ ); (d) snow surface retrieved from temperature difference between adjacent upper thermistors ( $\Delta T$ , solid curve) and acoustic sounding (dashed curve); (e) selected temperature profiles under different environmental conditions at times indicated in (a).

### 3.4. Snow Depth

Comparison of snow depths derived from temperature differences between adjacent thermistors ( $\Delta T$ ) in the upper part of the chain with those determined from the AWS acoustic sounder revealed generally similar patterns and features, despite the high snow-depth variability (Figure 4d). The large temperature differences in the top 0.2–0.3 m of the sea ice originated from the lack of refreezing in the part of the deployment hole above the sea surface. Snow depth was on average  $0.14 \pm 0.09$  m throughout the study. June exhibited by far the thickest snow cover,  $0.31 \pm 0.11$  m, with a maximum of 0.42 m. Snow depth before June was  $0.08 \pm 0.05$  m and  $0.16 \pm 0.06$  m afterward.

### 3.5. Snow/Ice Interface

The evolution of the snow/ice interface was best identified from the  $\delta T_{30}$  and  $\delta T_{120}$  profiles (Figures 4b and 4c). It was characterized by a high temperature difference of up to 2°C between adjacent thermistors in the

**Table 1.** Monthly Average Residual Heat Flux ( $F_w$ ) in  $W\ m^{-2}$  and Sea-Ice Thickness Increased ( $\Delta z_{si}$ ) in mm During the Study

| Monthly average       | 2012  |       | 2013 |       |       |       |       |       |       |       |       |       |       |       | 2014  |      | $\Sigma$ |
|-----------------------|-------|-------|------|-------|-------|-------|-------|-------|-------|-------|-------|-------|-------|-------|-------|------|----------|
|                       | Nov   | Dec   | Jan  | Feb   | Mar   | Apr   | May   | Jun   | Jul   | Aug   | Sep   | Oct   | Nov   | Dec   | Jan   | Feb  |          |
| Mean                  | -2.26 | -0.74 | 0.63 | -0.01 | -0.40 | -0.28 | -2.31 | -1.81 | -1.61 | -2.01 | -1.02 | -0.68 | -1.13 | -2.04 | -0.60 | 0.97 |          |
| Std                   | 0.44  | 1.45  | 0.30 | 0.13  | 0.07  | 0.32  | 1.11  | 0.64  | 0.45  | 0.68  | 0.57  | 0.84  | 0.83  | 0.48  | 0.81  | 0.09 |          |
| $\Delta z_{si}$ in mm | 20    | 46    | 5    | 1.2   | 4.4   | 49    | 147   | 113   | 101   | 140   | 132   | 123   | 95    | 74    | 32    | 0.01 | 1080     |
| % due to $F_w$        | 36    | 21    |      |       |       | 7     | 21    | 20    | 21    | 19    | 10    | 7     | 15    | 36    | 24    |      | 18       |

$\delta T_{120}$  data. This originated from the difference in thermal conductivity between snow and sea ice, which was about one order of magnitude. This interface was variable in height, differing by up to 0.3 m throughout the study. This was most likely again a consequence of the limited refreezing of the deployment hole, and does not reflect natural processes. However, the  $\delta T_{30}$  and  $\delta T_{120}$  profiles exhibited some interesting features near the snow/ice interface. During summer 2012/2013 and more pronounced in 2013/2014, areas with thermal characteristics that resemble the lower thermistors were apparent. It is likely that these were manifestations of meltwater formation and refreezing at the surface. Please note that the changing snow/ice interface described here is different from the reference snow/ice interface, which was assumed as constant for the calculation of snow depth and sea-ice thickness in this paper.

### 3.6. Ice/Water Interface

Isothermal conditions in the sea ice and the sub-ice platelet layer dominated the temperature profiles from January to May 2013, more than 1/3 of the year (Figure 4a). Under these circumstances, a determination of the ice/water interface from temperature measurements alone was impossible. However, the evolution of the ice/water interface was most pronounced in the  $\delta T_{120}$  profiles (Figure 4c, dashed white curve). For all further calculations in this study, we used an ice/water interface manually derived from the  $\delta T_{120}$  profiles. The resulting interface was additionally smoothed by a 10 day running mean to overcome the discrete distance between adjacent thermistors. During the study, the sea-ice thickness increased by 1.1 m, from 2.44 to 3.54 m. 0.1 m of this growth occurred between mid-November and mid-December 2012, when growth ceased for approximately 4 months. The remaining 1 m of growth occurred between mid-April 2013 and early January 2014. The average growth rate was  $0.0024 \pm 0.0017\ m\ d^{-1}$  over the entire study, and  $0.0033 \pm 0.0011\ m\ d^{-1}$  over the growth season only. The monthly sea-ice thickness increase is shown in Table 1.

### 3.7. Internal Melt and Refreezing

Several areas are present within the sea ice that exhibited a slightly higher  $\delta T_{30}$  and  $\delta T_{120}$  than the surrounding sea ice (Figures 4b and 4c, lighter blue). Due to the limited precision of the thermistors, these are difficult to identify. They are most likely indications of a phase transition from solid sea ice into the liquid phase, indicating internal melt. These structures were then altered by the advancing freezing front, which subsequently increased the solid fraction in the interior. This transition started approximately 0.5 m below the zero reference in February 2013. Shortly before April 2013, it was masked by the sea ice below, probably due to decreased melt in lower layers, leading to a reduction in the contrast. However, an artificial freezing front can be set to the bottom of the sea ice, marking the onset of active basal growth at the end of April 2013 (Figure 4b, dashed curve). Minor instances of different thermal characteristics inside the upper sea-ice layer were also apparent from January 2014, marking again the beginning of internal melt. Note that the freezing front (in contrast to the ice/water interface) may also be inferred from the temperature profiles (Figure 4a), by below-freezing temperatures which advanced through the sea-ice cover between February and April 2013.

### 3.8. Sub-ice Platelet Layer

TC-derived temperatures of the sub-ice platelet layer remained slightly below the freezing point throughout the study. Compared to simultaneous temperature measurements taken with a CTD75M (Sea and Sun Technology) in or near the platelet layer, thermistor temperatures were always lower. This is due to the thermistor's limited resolution causing a low signal-noise ratio given the very small temperature differences found in the seawater/platelet mixture. In order to interpret the heating data in the sub-ice platelet layer of Atka Bay (AB), it is useful to compare our results to measurements by an identical instrument in a sea-ice regime

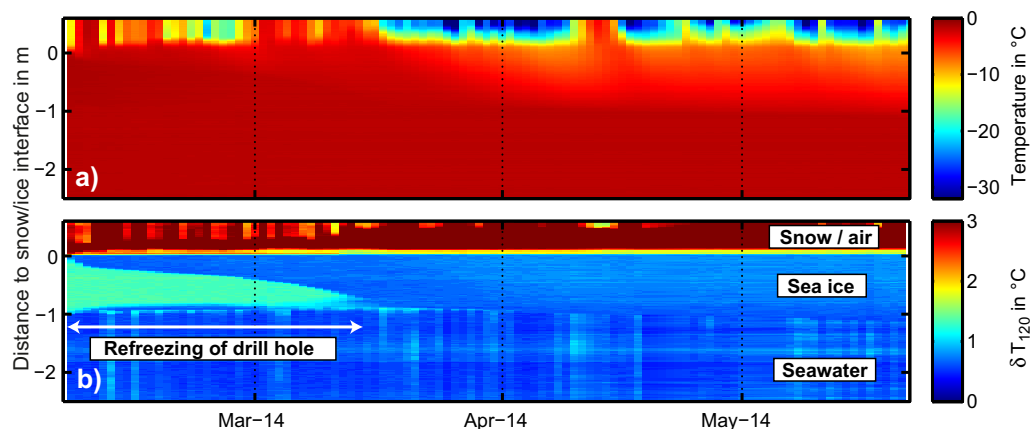


Figure 5. (a) Temperature and (b)  $\delta T_{120}$  profiles from a drifting thermistor chain in the central Weddell Sea.

without a platelet layer. Therefore, we chose to include a data set recorded in the central Weddell Sea (WS) in 2014 (Figure 5). It is immediately evident that the  $\delta T_{120}$  of sub-sea-ice thermistors at AB was  $\sim 0.5^\circ\text{C}$  higher than in the WS, which is nearly 10 times the stated precision. Between February and May 2013, this difference partly vanished in the lowermost thermistors. This could be an indication of either the presence of flowing seawater, or sea ice temporarily attaching itself to the chain. We will discuss this in greater detail later.

When closely investigated, the WS data set exhibits another striking feature. When a thermistor chain is installed, it usually takes a while for the hole to refreeze entirely, especially under warmer conditions. Such a refreezing front is clearly visible in the heating data depicted in Figure 5b. At the same time, the thermistors located in the deployment hole obviously detected different thermal characteristics than those in the ocean below, again reflecting the sensitivity of this approach to the flow velocity of a medium.

### 3.9. Conductive Heat Flux

Bulk conductive heat flux  $F_c$  was estimated for layers of 0.2 m thickness through the entire sea-ice cover according to equation (2). For the calculation of  $k_{si}(\rho, S, T)$ , we used a smoothed salinity profile based on Figure 3 and a sea-ice density of  $910 \text{ kg m}^{-3}$ . The average conductive heat flux was calculated between the actual snow/ice interface and the ice/water interface (Figure 6a).

The conductive heat flux near the snow/ice interface showed typical short-term fluctuations as a response to the rapid changes in the synoptic-scale atmospheric forcing, particularly air temperature. The absolute magnitude of  $F_c$  as well as the gradient generally decreased between upper and lower layers. The bottom layer lagged the induced variations in the upper sea-ice layer, which is most pronounced (up to 2 months) in autumn and spring. Apart from the expectedly low conductive heat flux in summer, several local minima also occurred during winter. These were especially apparent between August and October 2014, and are linked to relatively warm surface air advected to the site by passing synoptic systems (Figure 2). Another local minimum was observed during June 2013, lasting for more than 1 month. This was associated with a local maximum of snow cover (up to 0.4 m) described above. In contrast to the passage of the synoptic systems, this change of snow conditions also strongly affected the lower sea-ice layers.

Average  $F_c$  was low at the beginning of the study. Between December 2012 and February 2013, the temporal lag of warming in the sea-ice interior resulted in vertical temperature inversions and a subsequent negative  $F_c$ . This is a reflection of thermal energy transported into the sea-ice interior, downward at the top and upward at the base, leading to internal sea-ice warming and eventually also melt as described by *Lei et al.* [2014]. This condition was also observed between late December 2013 and February 2014. Typical vertical temperature inversion profiles are shown in Figure 4e (E1, E6, and E7). The average  $F_c$  increased gradually during atmospheric cooling in the transition from summer to winter (Figure 6b), reaching its absolute

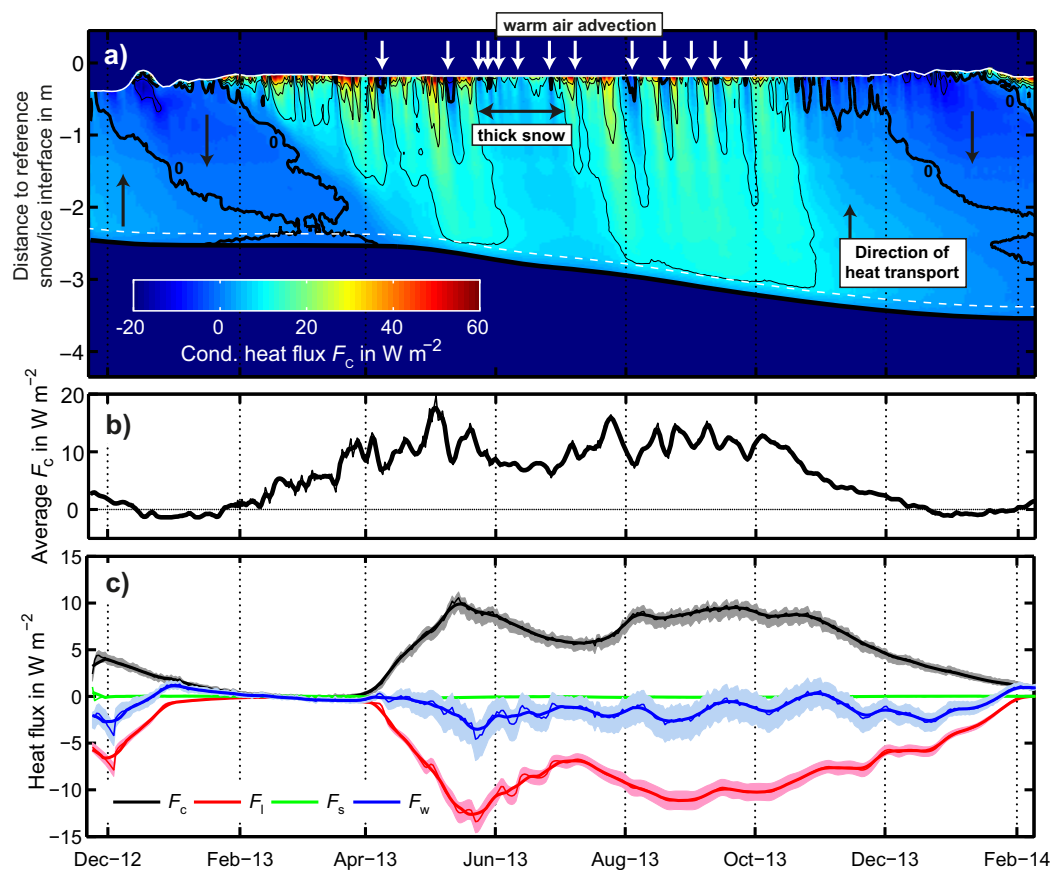


**Figure 6.** (a) Conductive heat flux through sea ice with contours at  $-20$ ,  $-10$ ,  $0$  (thick black curve),  $10$  and  $20 \text{ W m}^{-2}$ . Due to snow in the drill hole, the part between the reference snow/ice interface (zero) and the true snow/ice interface (solid white curve) was omitted. The white arrows correspond to the synoptic systems shown in Figure 2. (b) Average vertical conductive heat flux between the snow/ice interface and the ice/water interface. (c) Daily heat fluxes (thin curves) through a reference layer near the sea-ice base (dashed white curve in Figure 6a). The thick curves represent the 5 day running mean.  $F_c$  is the heat conducted upward through the reference layer,  $F_i$  is the latent heat required to form the thickness of sea ice added,  $F_s$  is the sensible heat flux which accounts for a temperature change in the reference layer, and  $F_w$  is the residual heat flux. The shaded areas represent the cumulative individual measurement uncertainties. Upward heat fluxes, warming and melting have a positive sign.

maximum of approximately  $20 \text{ W m}^{-2}$  in early May 2013. It then fluctuated around  $10 \text{ W m}^{-2}$ , until atmospheric warming from October 2013 as well as the increased sea-ice thickness again led to a gradual decrease.

### 3.10. Basal Energy Balance

In the basal energy balance (Figure 6c), upward heat fluxes, warming and melting have a positive sign, and shaded areas represent the overall uncertainties described below. The conductive heat flux through the reference layer ( $F_c$ , black) showed a similar pattern, although smoothed, to the vertically averaged conductive heat flux described above. The temperature change in the reference layer ( $F_s$ , green) was negligible. The (latent) heat removed to grow sea ice ( $F_i$ , red) roughly followed, but at the same time, exceeded the amount of heat conducted upward to the atmosphere and thus allowed for sea-ice thermodynamic growth. This resulted in a negative residual heat flux ( $F_w$ , blue) between  $-5$  and  $0 \text{ W m}^{-2}$  throughout the growth periods (November 2012 to January 2013, April 2013 to January 2014). The monthly averages of  $F_w$  are given in Table 1. On average, 18% of the sea-ice thickness gain during the study period was not accounted for by upward heat conduction (thermodynamic growth).

The overall uncertainties were estimated by cumulative variation of individual uncertainties in the measurements. Those were  $\pm 1$  for salinity,  $\pm 0.0625^\circ\text{C}$  for thermistor readings and  $\pm 25 \text{ kg m}^{-3}$  for the sea-ice density. Although the principal uncertainty in the retrieval of the ice/water interface is  $\pm 0.02 \text{ m}$ , the uncertainty in the running mean, which is used for the growth-rate calculation, is considered to be very small. Note that

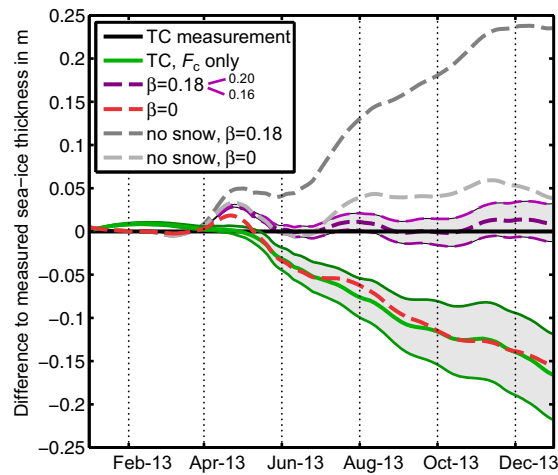


**Figure 7.** Comparison of sea-ice growth in 2013, derived from thermistor chain (TC) measurements and calculated from conductive heat flux alone (solid curves), along with results of different model simulations (dashed curves). The actual TC measurement (black line) is used as a zero reference. The upper half of the graph indicates thicker sea ice than this reference, the lower half indicates thinner sea ice. Filled areas represent a variation of ice-volume fraction  $\beta$  of  $\pm 0.02$  in the model (dashed violet curves), and the variation of the reference layer of  $\pm 0.02$  m for the calculation of the conductive heat flux (solid green curves).

snow depth and modified growth rates according to equation (5), and show here only the results for  $\beta = 0.16, 0.18,$  and  $0.20$  (violet curves, bottom to top). The best fit between simulated and observed thickness was achieved for  $\beta = 0.18$ . Uncertainties of  $\beta$  were discussed in detail in Hoppmann *et al.* [2015], and are estimated as approximately 0.10 mainly due to uncertainties in upward longwave radiation. Further model experiments without a snow cover and  $\beta = 0.18$  yielded a sea-ice thickness gain of 0.23 m (dashed, dark gray curve), while the combined absence of snow and platelets resulted in a net gain of 0.025 m (dashed, light gray curve).

Also shown is the adjusted growth rate  $\left(\frac{\partial H}{\partial t}\right)_{adj}$ , which was calculated from the basal energy balance only accounting for the conductive heat flux ( $F_w = 0$ , solid green curve):

$$\left(\frac{\partial H}{\partial t}\right)_{adj} = \frac{F_c + F_s}{\rho_{si} \cdot L_f}. \quad (6)$$

This generally represents a platelet-free scenario, and agrees well with the model result for  $\beta = 0$ . The uncertainties caused by a slight shift of the reference layer ( $\pm 0.02$  m, shaded area between green curves) are also given for illustration.

### 3.12. Sub-ice Platelet Layer Thickness

Part of the platelet-layer thickness data (Figure 8; November 2012 to February 2013) were already described in detail in Hoppmann *et al.* [2015] and are included here due to the overlapping study interval. The initial platelet-layer thickness was on average about 4 m at the beginning of this study, decreasing to 3 m in January and toward 2 m in February. This thinning was associated with the inflow of warm water. Although not many data points are available between February and April 2013 due to safety concerns, it is likely that a platelet layer of 1–2 m thickness survived the summer. The first measurements at the end of April revealed an average thickness of about 4 m (with a high variability), steadily increasing at all sites between June and December 2013. The average platelet accumulation at all sites between April and December was approximately 4 m, leading to a mean overall thickness of about 8 m. The highest annual thickness gain of 6 m was observed at ATKA11 (Figure 8b, black triangle), the highest absolute thickness of 10 m was measured at ATKA07 (white diamond) in October 2013. The seawater temperature below the northern ice shelf (Figure 8c) was below the surface freezing point between April and November 2013, with a minimum in late May. With the continuous inflow of relatively warm water at the end of November 2013, as determined from CTD

these considerations do not account for a variation of the reference layer and the range of thermistors used for calculation of the temperature gradient, both of which move the curves upward and downward, and therefore have substantial influence on the residual flux.

### 3.11. Model Results and Ice-Volume Fraction

The results of different model runs (dashed curves) are shown in Figure 7, where the actual sea-ice thickness as determined from TC heating profiles is used as a zero reference. A positive sea-ice thickness difference (upper part of the graph) means thicker sea ice than observed, and vice versa.

Simulated sea-ice thickness with an unmodified growth rate and TC snow depth ( $\beta = 0$ , dashed red curve) differed from the observed sea-ice thickness by about 0.15 m at the end of growth. We performed additional model simulations with measured

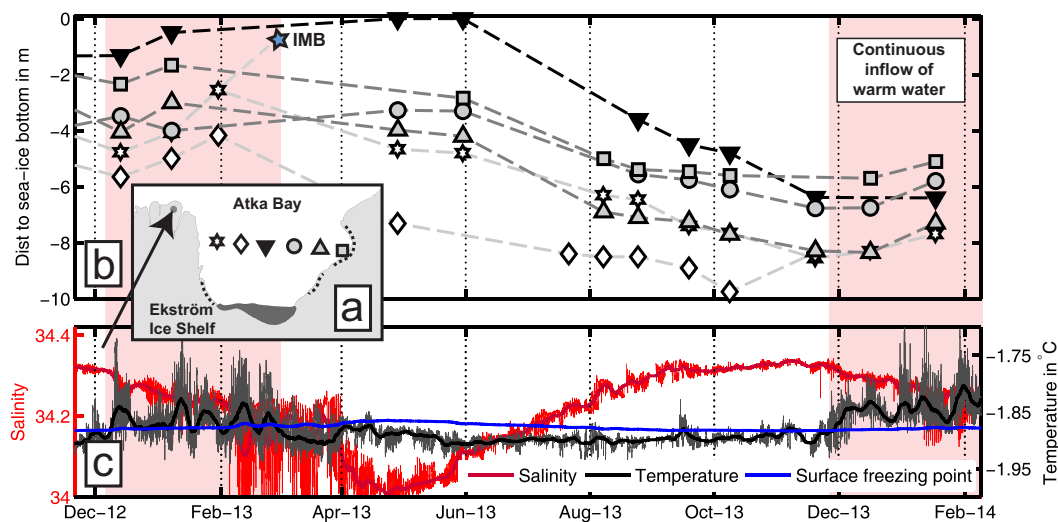


**Figure 8.** Platelet-layer thickness at the six sites between 2012 and 2014, along with oceanographic conditions recorded at a measurement site below the Ekström Ice Shelf. (a) Coarse map of the study area. The dark gray and dashed curves represent ice rises and rumples, respectively. (b) Sub-ice platelet-layer thickness evolution at different study sites, with symbols corresponding to their location according to Figure 8a. The blue star indicates the likely platelet-layer thickness determined by the IMB. (c) Seawater salinity (red) and temperature (black) measured by the MicroCAT at a depth of 155 m, at full resolution (thin curves) and 7 day running mean (thick curves). The corresponding surface freezing point is given in blue. The shaded area indicates the continuous inflow of relatively warm water.

measurements under the sea ice, the platelet-layer thickness again started to decrease. The time series stops shortly before the fast-ice breakup on 9 February 2014.

## 4. Discussion

In the first part of the discussion, we focus on the following factors that influenced the properties of the fast-ice cover and its basal energy balance in our study: (1) the general atmospheric conditions and the passage of synoptic systems, (2) the snow cover, (3) near-surface seawater temperatures, and (4) the properties of the sub-ice platelet layer. Combining all our results, we finally provide a schematic diagram depicting the seasonal evolution of fast ice in Atka Bay (2012–2014) near the Ekström Ice Shelf. In the second part, we discuss the potential of the instrument on the basis of this unique data set, and point out several limitations.

### 4.1. Seasonal Cycle of Fast Ice near an Ice Shelf

Since the sea-ice bottom was always near or at the freezing point (Figure 4a), near-surface air temperatures and snow depth governed the overall sea-ice temperature gradient, and with it the conductive heat flux. While the recurrent passage of relatively warm synoptic systems (Figure 2) strongly modified the temperature gradient in the upper part of the sea ice, these relatively rapid changes barely influenced the sea-ice bottom (Figure 6a). This is mainly due to the large thickness of the second-year sea ice and therefore these conditions did not influence the conductive heat flux through the near-bottom reference layer (Figure 6c). In contrast, the atmospheric conditions determined the presence of precipitation and snow drift, which play a crucial role in the evolution of a sea-ice cover through the low thermal conductivity of the snow. The strong insulating effect was particularly apparent in June and July 2013, when snow depth was at its maximum of up to 0.4 m (Figure 4e). With a delay of several weeks, this effect led to a drastic reduction of the temperature gradient, and consequently the sea-ice growth rate. As also shown in our model simulations, snow depth had a substantial influence on overall sea-ice growth. When comparing model runs with the measured snow depth throughout 2013 to a snow-free scenario, the sea-ice thickness at the end of the growth season was reduced by 23% (Figure 7). Unfortunately, ATKA03 was in the lee of an iceberg 2 km to the east (Figure 1), leading to a strong modification of snow deposition. The evolution of the snow cover shown here, with an average of 0.14 m, is therefore not representative for Atka Bay in general, which exhibited a significantly higher overall snow depth. A more realistic snow cover, derived from snow measurements on transects across Atka Bay at 1 km intervals, yielded bay-wide averages of 0.3 m in April, to 1.3 m in December 2013 (not shown). A corresponding model simulation with a linearly increasing snow cover revealed a sea-ice thickness increase of only 0.58 m (not shown), including a contribution from ice platelets. The observed

sea-ice growth of 1.1 m over this study (corresponding to 1 m in 2013) is therefore considered significantly above-average.

The presence of in situ supercooling in and in front of the ice-shelf cavity, also referred to as (supercooled) Ice Shelf Water plumes, [Robinson *et al.*, 2014], determines the formation of ice platelets [Lewis and Perkin, 1986]. As we do not have near-surface ocean data available at depths where in situ supercooling is most likely to occur [Smith *et al.*, 2001], we consider the presence of potentially supercooled water as an indicator for potential ice-platelet formation. Since the sub-ice shelf seawater temperature was consistently below the surface freezing point between late April and December 2013, and with higher variability even earlier (Figure 8b), platelet formation is possible throughout. Hoppmann *et al.* [2015] showed that in Atka Bay a sub-ice platelet layer starts to form during June. In contrast, results from our sea-ice texture analysis suggest that small platelets already modified the sea-ice texture up to two months earlier, although we cannot identify the exact timing from our measurements (Figure 3c). This is explained by the fact that the freezing interface in the early stage of formation may outgrow the comparably slow platelet accumulation [Dempsey *et al.*, 2010]. This hypothesis is also confirmed by the pattern of platelet-layer thickness evolution in 2013, which showed already a net increase between February and May (Figure 8). It is unclear if this is the results of new accumulation or just redistribution from sites closer to the ice shelf with higher platelet-layer thickness. However, our results confirm the pattern of seasonal platelet-layer thickness evolution as found in Hoppmann *et al.* [2015], although a higher rate of thickness increase suggests the presence of strong platelet redistribution by currents directly under the sea ice. This has to be taken into account when interpreting platelet-layer thickness data in years where the fast ice did not break out completely during the previous summer. As soon as warm Antarctic Surface Water reaches the ice-shelf front in November/December [Hattermann *et al.*, 2012], the platelet layer thinned at a rate of approximately  $1 \text{ m month}^{-1}$  (Figure 8b). Using an ice-volume fraction of 0.18, as found in the present study, this roughly corresponds to an oceanic heat flux of  $+21 \text{ W m}^{-2}$ , in accordance with observations on fast ice in other regions [Heil *et al.*, 1996; Lei *et al.*, 2010]. At the same time, melting of the solid sea ice only occurred to a minor degree at the surface and in the ice interior (Figure 4). Despite the relatively high summer temperatures (Figure 2a), the increased radiative heating and the high oceanic heat flux, thermodynamic sea-ice growth even continued until the end of the study, albeit slowly (Figures 4b and 4c). This is due to the platelet layer shielding the sea ice from below and the slow temporal progression of the  $0 \text{ W m}^{-2}$  contour in the conductive heat flux (Figure 6a) due to the large sea-ice thickness.

According to the basal energy balance, about 18% (0.2 m) of the overall sea-ice growth (1.1 m) originated from a residual heat flux. The selection of the reference level and the number of thermistors for the linear fit of the temperature gradient may alter this result significantly. However, if the reference level is shifted, results for which this residual heat flux becomes positive, especially during the growth season, are implausible. It can therefore be safely assumed that the residual heat flux should be  $<0 \text{ W m}^{-2}$  until at least mid-November. The negative residual heat flux can be interpreted as a representation of the ice crystals just below the advancing freezing interface [Gough *et al.*, 2012]. These reduce the amount of heat that needs to be transported upward in order to grow a certain sea-ice thickness. In this interpretation, our results translate into an ice-volume fraction  $\beta$ , of 0.18. In order to provide an uncertainty estimate,  $\beta$  can also be calculated inserting equation (6) into equation (5) as a platelet-free growth rate:

$$\beta = 1 - \frac{F_c + F_s}{F_1} \quad (7)$$

Averaging over the active sea-ice growth (May–January) results in  $F_c = 7.06 \pm 2.08 \text{ W m}^{-2}$ ,  $F_1 = -8.5 \pm 2.24 \text{ W m}^{-2}$ , and  $F_s = -0.06 \pm 0.05 \text{ W m}^{-2}$ . According to equation (7), and using Gaussian error propagation, this corresponds to  $\beta = 0.18 \pm 0.09$ .

In an independent approach, our model simulations with local atmospheric forcing and a variable growth rate reproduced the observed sea-ice thickness evolution best with a  $\beta = 0.18$  (Figure 7). In addition to the good agreement of this independent approach to our residual flux calculation, this result also agrees well with the findings of Kipfstuhl [1991] and especially Hoppmann *et al.* [2015], who simulated sea-ice growth at several study sites with the same model setup, but with forcing data and independent observations (drillings) for the year 2012. Their result for ATKA03, the site of the present study, agrees within error, giving further confidence in our results, the performance of the model and the quality of the forcing data. Using a similar approach, Gough *et al.* [2012] found in their study an ice-volume fraction of  $0.25 \pm 0.06$ . The

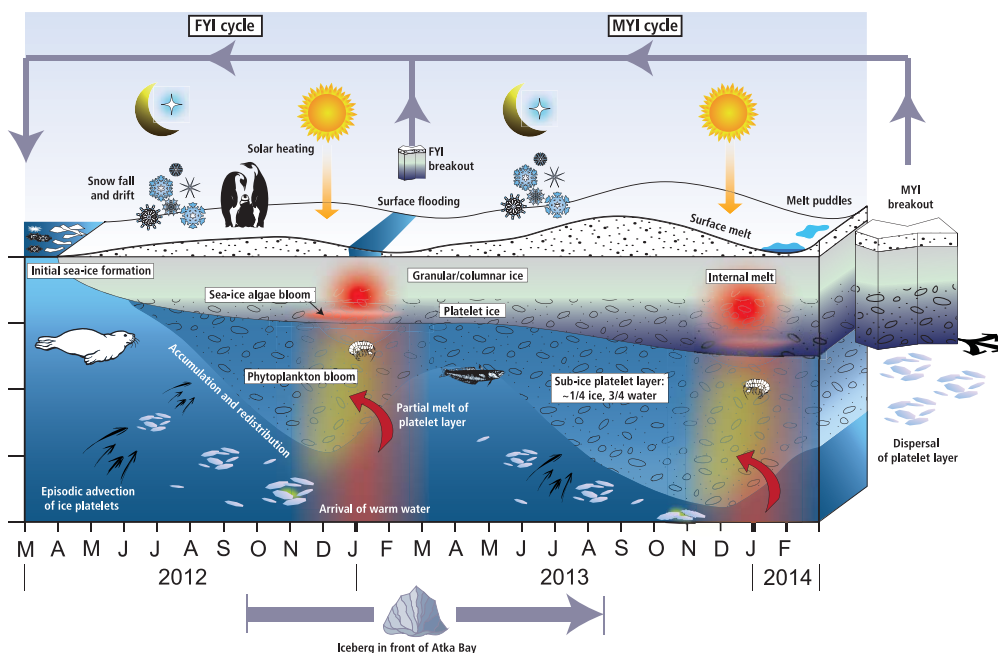


**Figure 9.** Schematic diagram of the seasonal cycle of Atka Bay fast ice and the sub-ice platelet layer, based on results of Hoppmann *et al.* [2015] for 2012 and this study for 2013/2014.

difference could be a reflection of the different TC setup, or more likely, the spatiotemporal variability in the platelet layer itself. It is for example currently unclear how the crystal-size distribution depends on the geographical setting and the time of the year, and how this potentially modifies the ice-volume fraction.

According to Hoppmann *et al.* [2015], accumulation and incorporation of platelets lead to an overall contribution to first-year sea-ice mass of about 50% in Atka Bay. Here we extend this result to multiyear sea ice: the platelet-layer thickness at ATKA03 increased by about 7 m, from approximately 1.5 m in February to 8.5 m in December. With  $\beta = 0.18$ , this corresponds to an effective sea-ice thickness of 1.26 m, or 60% of the combined solid and “loose” sea ice in 2013 (2.1 m). Including the amount that is already frozen into the sea ice (0.2 m), the overall oceanic contribution at the study site is 1.46 m, or 70% of the overall sea-ice thickness. This is considered an upper limit since it is unknown how much platelets were actually just redistributed from other locations.

It may also be useful to recalculate these results for the estimated bay-wide averages. The effective sea-ice thickness increase represented by the platelet layer is  $4 \text{ m} \times 0.18 = 0.72 \text{ m}$ . An estimation for the average sea-ice growth with incorporated platelets was already calculated earlier from a model simulation using bay-wide measurements of snow cover (0.58 m). Multiplication with  $\beta$  yields an effective sea-ice thickness from incorporated platelets of 0.10 m, with a thermodynamic growth of 0.48 m. Using these numbers, the contribution of ice platelets to the annual sea-ice thickness increase becomes 63%, or nearly 2/3. Taking into account a specific area and a defined sea-ice density, this result may be directly translated into sea-ice mass or volume. This result thereby shows that in areas where sea ice grows slowly, such as multiyear sea ice or where a thick snow cover is present, much of the sea-ice volume gained is a direct result of ocean/ice-shelf interaction in nearby cavities.

Finally, we present a schematic diagram (Figure 9) mainly incorporating findings from the present study and from Hoppmann *et al.* [2015], to summarize the seasonal evolution of the fast-ice regime of Atka Bay.

Although our study provided a further piece in the puzzle of how the physical environment of a fast-ice regime affected by platelet accumulations behaves and evolves over time, the major challenge is now to unravel its implications for the associated ecosystem and to identify the linkages between different trophic levels, such as micro algae [Dieckmann *et al.*, 1986; Günther and Dieckmann, 1999], invertebrates [Günther *et al.*, 1999], notothenioid fish [La Mesa *et al.*, 2004; Vacchi *et al.*, 2004], seals [Davis *et al.*, 1999], and penguins [Zitterbart *et al.*, 2014].

#### 4.2. Assessment of the Instrument's Potential

Sea-ice mass balance buoys have been an important tool in sea-ice research in the recent past, and they remain crucial to monitor changes in the polar oceans. However, commonly used IMBs are too expensive to be deployed in large numbers, which would be needed to assess the large-scale changes and to identify responsible processes. The main difference between the TC used here and other, well established IMBs [Richter-Menge *et al.*, 2006], is the lack of acoustic sounders above the snow surface and below the sea-ice bottom. The simpler construction allows for easy deployment, taking one person about 30 min. At the same time, it is however difficult to infer the interfaces between air, snow, sea ice and seawater from temperature profiles alone. Based on our data, the main questions we try to address are: (1) How well is the heating mode able to compensate the loss of information due to the lack of acoustic sounders? (2) Which additional information about a sea-ice cover can be inferred from the heating data?

Due to the large air temperature fluctuations typically observed in polar regions, the temperature gradient near the upper snow surface is substantial. In contrast, thermistors in the air usually measure the same temperature (within their accuracy). Consequently, the air/snow interface, and hence the snow depth, may be inferred from temperature differences between adjacent thermistors. Although the heating profiles generally indicated a similar snow-depth evolution, the highest difference in temperature response between adjacent thermistors was generally located a few centimeters below the air/snow interface determined from temperature profiles. We explain this by the fact that the wind moves the upper part of the chain, creating an air gap around the upper few thermistors. Due to the lack of contact area, these thermistors then record the same characteristics as those in the air above. This effect did not influence the temperature measurements to a comparable degree. As a result, the temperature measurements provide a better indication of snow depth than the heating profiles, which reproduce the general pattern but underestimate snow depth by up to 0.1 m. In summer, the retrieval of the air/snow interface is additionally influenced by radiative warming of the chain, an effect which we have neglected here.

As stated earlier, the temperature response to a defined heat input is generally proportional to the thermal conductivity and specific heat capacity of a medium. The difference between  $\delta T_{120}$  and  $\delta T_{30}$  was close to zero for sea ice, around 0.1 K for the platelet/water mixture and some regions in the sea-ice interior, and up to 4 K for snow and air (not shown). For sea ice it was therefore not possible to derive a plausible thermal conductivity from these data, mainly because the measurements at 30 and 120 s were not in the linear part of the temperature rise curve. Although a calculation should in principal be possible for snow, the complex geometry of the sensors modifies the typical equations used for needle-probe measurements, and a detailed investigation was beyond of the scope of this paper.

Through the 10-fold difference in thermal conductivity of sea ice and snow, the snow/ice interface is sharply pronounced in the heating profiles and easily extracted. This is also true for the air/ice interface in the absence of snow. However, the evolution of the sea-ice surface is admittedly more interesting in the presence of surface melt, which is more pronounced in the Arctic compared to the Antarctic. To our knowledge, no study has yet been published using the heating mode of the TC to infer the evolution of surface melt and the formation of a melt pond. However, it has been shown above that determining a (nonflowing) ice/water interface is very promising with this method, provided only diffusive heat transfer is likely to take place. This should be the case for surface meltwater. Since it is expected that the location of an air/water interface is also easily determined, this approach is promising to monitor melt-pond depth evolution, and even refreezing (under the assumption that the instrument stays in place).

When calculating a sea-ice mass budget, internal melt processes are usually neglected due to the lack of a suitable methodology. As described above, several areas in the heating data sets can be interpreted as internal melt or even the formation of gap layers. These mainly occurred in summer, most prominently between February and April 2013. Although we do not study these in detail here, this potentially provides additional insight into melt processes.

In our case, the heating data effectively provided 3 months of additional information about the evolution of the ice/water interface, mainly for isothermal conditions in summer 2013. However, such a clear identification was only possible due to a presence of a sub-ice platelet layer. Sea ice and flowing water exhibit a similar thermal response to an applied heating. Under flowing conditions, the ice/water interface may still be inferred from the variations of flow speed of the underlying water, which results in slightly variable

temperature differences. This behavior was also described in *Jackson et al.* [2013], and is indicated in the Weddell Sea data set as different shades of blue (Figure 5b). However, this effect significantly complicates the implementation of general algorithms to automatically retrieve the ice/water interface. In addition, a longer time series is needed to accurately interpret the subtle differences not visible from few measurements alone, noting a higher measurement frequency might also assist. Furthermore, Figure 5b demonstrates that the thermal characteristic of refreezing in the upper borehole differ from those of the surrounding medium. According to the scenario described above, this is most likely explained by a near-zero flow rate in the drill hole, in contrast to the ocean below.

This effect leads to an interesting application of this instrument in sea-ice regimes with a sub-ice platelet layer: dealing with supercooled seawater and associated processes, temperature differences in the order of several mK need to be resolved. This prerequisite is not met by the thermistors embedded in the chain. However, although the platelet layer is highly porous, it is safe to assume that the geometric properties of the platelet matrix impede the oceanic currents enough to significantly reduce the flow. Comparison of the Atka Bay (Figure 4c) and the Weddell Sea data sets (Figure 5b) suggest that it is therefore in principle possible to distinguish a sub-ice platelet layer from an unimpeded seawater flow. If this hypothesis holds, we are now able to interpret the darker blue areas below the sea-ice base from February to June 2013 (Figures 4b and 4c) as a temperature response associated with thinning and reconsolidation processes in the platelet layer. The thinning, or more specifically, the presence of ice-free, flowing seawater surrounding the lowermost thermistors in March is consistent with results from manual platelet-layer thickness measurements at ATKA03 (Figure 8b, star symbols), because further bottom melt is expected as long as relatively warm water is present until the beginning of March (Figure 8c). Between March and the beginning of May 2013, the data quality is too low due to artifacts caused by power issues. In mid-May, the lowermost thermistors exhibit a sudden increase in their temperature response, showing a signature similar to that before platelet-layer melt (especially visible in Figure 4c). This is again consistent with Figure 8b, in that our drillings showed the platelet-layer thickness had already increased to more than 4 m in April. This was seemingly not reproduced by the IMB data. However, a closer investigation of Figures 4b and 4c reveals that the temperature response of the lower thermistors in the first half of May was slightly different from that observed in March. We interpret this as a signature of the early phase of platelet-layer establishment, where the connectivity in the interstitial water is still high enough to allow for a detectable flow rate. The rapid transition in mid-May would then correspond to an enhanced consolidation, reduced connectivity and consequently, reduced flow rates. These results suggest that the heating mode is able to detect the platelet-layer bottom, although the possibility of the lower thermistors simply being encased in platelet ice cannot be ruled out entirely.

The most important constraint to this application, as also shown in our study, is the chain length. Although a typical thermistor chain length of 4.8 m seems long enough for a deployment in typical sea ice, it is too short to also monitor the evolution of a platelet layer over the course of winter, which can well reach up to 10 m. In our case, a length of about 10 m (with a wider thermistor spacing in the lower 5 m) would be needed to cover the entire seasonal cycle. But as the shear stresses on such a long chain increase dramatically due to the strong under-ice currents, the risk of a failure is high. Further testing is necessary to assess if such a long chain is practical. In addition, an IMB equipped with an acoustic sounder below the sea ice is generally not suited to be operated in areas where a sub-ice platelet layer is present or expected. Objects or instruments hanging below the sea ice serve as an ideal body for large amounts of ice crystals to grow on, a phenomenon for example photographed by *Mahoney et al.* [2011]. Even if the sensor would remain ice-free, a detection of the sea-ice/platelet layer interface would rely on temperature measurements alone, leading to higher uncertainties.

As usual, there are also several difficulties and problems associated with the operation of such an instrument. Here we identify some issues we experienced which the user needs to be aware of. The obvious is that predeployment calibration and testing is crucial to characterize the instrument.

The prominent vertical structures in Figures 4b and 4c are a result of a drop in voltage applied to the resistors during heating, which is usually 8 V. This effect leads to less pronounced contrasts between different media and occurred whenever the general battery voltage dropped below 10 V. It affected roughly 1/3 of the heating profiles. However, the other measurements were still sufficient for an accurate determination of interfaces between different media. The temperature profiles, and therefore all energy balance calculations,

are not impacted at all by this effect. For a calculation of thermal properties (not shown here), this effect has to be taken into account. The heating voltage is usually also recorded, and is included in the status message when operated via Iridium.

In order to obtain a continuous time series of snow depth throughout a certain study, a part of the thermistor chain has to remain above the snow surface (Figure 4b). The chosen length of this segment depends on the expected snow accumulation in a study region, and the construction of a suitable rack. In our study, 0.5 m above the snow surface was just enough to keep track of the snow-depth evolution. Under conditions of  $>0.5$  m snow accumulation, continuous snow-depth retrieval is therefore difficult. In addition, the surface unit is quickly buried under the thick snow, and data transmission is potentially hampered when the snow becomes too thick or wet.

Our data processing, the development of algorithms and the setting of thresholds was tuned to fit the presented data set. Since the heating profiles strongly depend on a combination of the thermal characteristics of a medium and its flow speed, the presentation of a generally applicable procedure to infer the different interfaces for other sea-ice data sets is difficult and beyond the scope of this paper. However, with a quickly increasing number of such data sets, we identify the need for a set of generally applicable algorithms to facilitate speedy and unified data processing and interpretation.

## 5. Summary and Conclusion

Measurements of the atmosphere, sea ice, ocean, and sub-ice platelet layer have been made on Antarctic first/second-year fast ice over 15 month. The grounding of a large iceberg in front of Atka Bay, which prevented a usual sea-ice breakup in 2013, presented a unique opportunity to perform a continuous and detailed study of the sea-ice processes, and especially the sub-ice platelet-layer evolution, over such a long period. The main data set presented here is a consistent time series of air, snow, sea-ice, and ocean/platelet-layer temperature profiles recorded by a thermistor chain which is also able to actively heat resistor components mounted near the temperature sensors. This data set is one of the longest of its kind recorded to date, and highlights various features in the seasonal sea-ice evolution.

It is supplemented by simultaneous, consistent time series of sub-ice-shelf temperatures and salinities, and high quality meteorological data partly obtained directly next to the thermistor chain. The total solid sea-ice thickness gain during 2013 was about 1 m, due to the high initial thickness of 2.5 m and the snow cover that was thick for some of the time. In total, 18% of the ice grown between April and December 2013 was not accounted for by heat conduction to the atmosphere. The translation of this result to a platelet-layer ice-volume fraction of  $0.18 \pm 0.09$  was also confirmed by independent sea-ice growth simulations, which yielded an ice-volume fraction of  $0.18 \pm 0.10$ . The platelet-layer thickness near ATKA03 increased by about 7 m (from 1.5 to 8.5 m) in 2013, with a bay-wide average of about 4 m. Overall, oceanic contribution to sea-ice thickness accounted for up to 70% of the total thickness. We showed that an approximate oceanic heat flux of  $21 \text{ W m}^{-2}$  during summer months is not sufficient to melt the entire platelet layer. Therefore, our study directly supplies evidence that in areas where sea ice grows slowly, such as thick multiyear sea ice or in the presence of a thick snow cover, most of the ice volume is contributed by ocean/ice-shelf interaction.

We also showed that, by the distinction of media through their thermal properties and flow speed, the heating mode is able to compensate the lack of acoustic sounders present on standard IMBs. This makes this buoy far easier to deploy and more reliable. By careful extraction of the interfaces from both measurement modes, it is possible to accurately determine the basal energy budget. In addition, the instrument is able to resolve internal structures such as gap layers and their refreezing. Although it is generally possible to derive the thermal conductivity and specific heat capacity of sea ice and snow with this approach, their quantification was beyond the scope of this work.

Finally, our study supplied evidence that a thermistor chain with active heating is capable of detecting the sub-ice platelet layer thickness through the lower current speed compared to the underlying ocean. Thereby it is currently the only automated method to continuously monitor the formation of a sub-ice platelet layer. This makes it the ideal tool to study sea-ice regimes influenced by ocean/ice-shelf interaction continuously over an extended time.

**Acknowledgments**

The authors are most grateful to the Neumayer III overwintering teams in 2012 and 2013 for their support in the field. We acknowledge Lars Kindermann and Olaf Boebel for the CTD data, and Sandra Schwegmann for the buoy deployment. Our research at Neumayer III and onboard RV Polarstern ANT-XXIX/9 would not have been possible without the help of the crew and the AWI logistics. This work was supported by the German Research Council (DFG) in the framework of the priority programme "Antarctic Research with comparative investigations in Arctic ice areas" by grants to SPP1158, NI 1092/2 and HE2740/12, and the Alfred-Wegener-Institut Helmholtz-Zentrum für Polar- und Meeresforschung. The data used here are publicly available at <http://doi.org/10.1594/PANGAEA.833978>. PH was supported under AAS grant #4301 and by the Australian Government's Cooperative Research Centre's Program through the Antarctic Climate and Ecosystems Cooperative Research Centre. Finally, the authors are grateful to two anonymous reviewers whose constructive comments significantly improved this manuscript.

**References**

Arrigo, K. R., D. H. Robinson, and C. W. Sullivan (1993), A high-resolution study of the platelet ice ecosystem in McMurdo Sound, Antarctica: Photosynthetic and bio-optical characteristics of a dense microalgal bloom, *Mar. Ecol. Prog. Ser.*, *98*(1–2), 173–185, doi:10.3354/meps098173.

Bintanja, R., G. J. van Oldenborgh, S. S. Drijfhout, B. Wouters, and C. A. Katsman (2013), Important role for ocean warming and increased ice-shelf melt in Antarctic sea-ice expansion, *Nat. Geosci.*, *6*, 376–379, doi:10.1038/ngeo1767.

Bintanja, R., G. J. van Oldenborgh, and C. A. Katsman (2015), The effect of increased fresh water from Antarctic ice shelves on future trends in Antarctic sea ice, *Ann. Glaciol.*, *56*(69), 120–126.

Bitz, C. M., and W. H. Lipscomb (1999), An energy-conserving thermodynamic model of sea ice, *J. Geophys. Res.*, *104*(C7), 15,669–15,677, doi:10.1029/1999JC900100.

Boebel, O., L. Kindermann, H. Klinck, H. Bornemann, J. Plötz, D. Steinhage, S. Riedel, and E. Burkhardt (2006), Real-time underwater sounds from the Southern Ocean, *Eos Trans. AGU*, *87*(36), 361, doi:10.1029/2006EO360002.

Davis, R. W., L. A. Fuiman, T. M. Williams, S. O. Collier, W. P. Hagey, S. B. Kanatous, S. Kohin, and M. Horning (1999), Hunting behavior of a marine mammal beneath the Antarctic fast ice, *Science*, *283*(5404), 993–996, doi:10.1126/science.283.5404.993.

Dempsey, D. E., P. J. Langhorne, N. J. Robinson, M. J. M. Williams, T. G. Haskell, and R. D. Frew (2010), Observation and modeling of platelet ice fabric in McMurdo Sound, Antarctica, *J. Geophys. Res.*, *115*, C01007, doi:10.1029/2008JC005264.

Dieckmann, G., G. Rohardt, H. Hellmer, and J. Kipfstuhl (1986), The occurrence of ice platelets at 250 m depths near the Filchner Ice Shelf and its significance for sea ice biology, *Deep Sea Res., Part A*, *33*(2), 141–148, doi:10.1016/0198-0149(86)90114-7.

Eicken, H., and M. A. Lange (1989), Development and properties of sea ice in the coastal regime of the southeastern Weddell Sea, *J. Geophys. Res.*, *94*(C6), 8193–8206, doi:10.1029/JC094iC06p08193.

Fahrbach, E., S. Harms, G. Rohardt, M. Schröder, and R. A. Woodgate (2001), Flow of bottom water in the northwestern Weddell Sea, *J. Geophys. Res.*, *106*(C2), 2761–2778, doi:10.1029/2000JC900142.

Fichefet, T., and M. A. M. Maqueda (1999), Modelling the influence of snow accumulation and snow-ice formation on the seasonal cycle of the Antarctic sea-ice cover, *Clim. Dyn.*, *15*(4), 251–268, doi:10.1007/s003820050280.

Fraser, A. D., R. A. Massom, K. J. Michael, B. K. Galton-Fenzi, and J. L. Lieser (2012), East Antarctic landfast sea ice distribution and variability, 2000–08, *J. Clim.*, *25*(4), 1137–1156, doi:10.1175/JCLI-D-10-05032.1.

Gough, A. J., A. R. Mahoney, P. J. Langhorne, M. J. M. Williams, N. J. Robinson, and T. G. Haskell (2012), Signatures of supercooling: McMurdo Sound platelet ice, *J. Glaciol.*, *58*(207), 38–50, doi:10.3189/2012JoG10J218.

Günther, S., and G. S. Dieckmann (1999), Seasonal development of algal biomass in snow-covered fast ice and the underlying platelet layer in the Weddell Sea, Antarctica, *Antarct. Sci.*, *11*(3), 305–315, doi:10.1017/S0954102099000395.

Günther, S., and G. S. Dieckmann (2001), Vertical zonation and community transition of sea-ice diatoms in fast ice and platelet layer, Weddell Sea, Antarctica, *Ann. Glaciol.*, *33*(1), 287–296, doi:10.3189/172756401781818590.

Günther, S., M. Gleitz, and G. S. Dieckmann (1999), Biogeochemistry of Antarctic sea ice: A case study on platelet ice layers at Drescher Inlet, Weddell Sea, *Mar. Ecol. Prog. Ser.*, *177*, 1–13.

Hattermann, T., O. A. Nøst, J. M. Lilly, and L. H. Smedsrud (2012), Two years of oceanic observations below the Fimbul Ice Shelf, Antarctica, *Geophys. Res. Lett.*, *39*, L12605, doi:10.1029/2012GL051012.

Heil, P. (2006), Atmospheric conditions and fast ice at Davis, East Antarctica: A case study, *J. Geophys. Res.*, *111*, C05009, doi:10.1029/2005JC002904.

Heil, P., I. Allison, and V. I. Lytle (1996), Seasonal and interannual variations of the oceanic heat flux under a landfast Antarctic sea ice cover, *J. Geophys. Res.*, *101*(C11), 25,741–25,752, doi:10.1029/96JC01921.

Heil, P., S. Gerland, and M. A. Granskog (2011), An Antarctic monitoring initiative for fast ice and comparison with the Arctic, *Cryosphere Discuss.*, *5*(5), 2437–2463, doi:10.5194/tcd-5-2437-2011.

Holland, P. R., and R. Kwok (2012), Wind-driven trends in Antarctic sea-ice drift, *Nat. Geosci.*, *5*, 872–875, doi:10.1038/ngeo1627.

Hoppmann, M., et al. (2015), Ice platelets below Weddell Sea land fast sea ice, *Ann. Glaciol.*, *56*(69), 175–190, doi:10.3189/2015AoG69A678, in press.

Hunkeler, P., S. Hendricks, M. Hoppmann, S. Paul, and R. Gerdes (2015), Towards an estimation of sub-sea-ice platelet-layer volume with multi-frequency electromagnetic induction sounding, *Ann. Glaciol.*, *56*(69), 137–146, doi:10.3189/2015AoG69A705.

Jackson, K., J. Wilkinson, T. Maksym, J. Beckers, C. Haas, D. Meldrum, and D. Mackenzie (2013), A novel and low cost sea ice mass balance buoy, *J. Atmos. Oceanic Technol.*, *30*, 2676–2688, doi:10.1175/JTECH-D-13-00058.1.

Jeffries, M. O., W. F. Weeks, R. Shaw, and K. Morris (1993), Structural characteristics of congelation and platelet ice and their role in the development of Antarctic land-fast sea-ice, *J. Glaciol.*, *39*(132), 223–238.

Kawamura, T., K. I. Ohshima, T. Takizawa, and S. Ushio (1997), Physical, structural and isotopic characteristics and growth processes of fast sea ice in Lützow-Holm Bay, Antarctica, *J. Geophys. Res.*, *102*(C2), 3345–3355, doi:10.1029/96JC03206.

Kipfstuhl, J. (1991), Zur Entstehung von Unterwassereis und das Wachstum und die Energiebilanz des Meereises in der Atka Bucht, Antarktis, *Ber. Polarforsch.*, *85*, 88 pp., doi:10013/epic.10085.d001.

König-Langlo, G., and B. Loose (2007), The meteorological observatory at Neumayer Station (GvN and NM-II) Antarctica, *Polarforschung*, *76*, 25–38.

König-Langlo, G., J. C. King, and P. Pettré (1998), Climatology of the three coastal Antarctic stations Dumont d'Urville, Neumayer, and Halley, *J. Geophys. Res.*, *103*(D9), 10,935–10,946, doi:10.1029/97JD00527.

La Barbara, M., and S. Vogel (1976), An inexpensive thermistor flowmeter for aquatic biology, *Limnol. Oceanogr.*, *21*, 750–756.

La Mesa, M., J. T. Eastman, and M. Vacchi (2004), The role of notothenioid fish in the food web of the Ross Sea shelf waters: A review, *Polar Biol.*, *27*(6), 321–338, doi:10.1007/s00300-004-0599-z.

Lefebvre, W., and H. Goosse (2008), An analysis of the atmospheric processes driving the large-scale winter sea ice variability in the Southern Ocean, *J. Geophys. Res.*, *113*, C02004, doi:10.1029/2006JC004032.

Lei, R., Z. Li, B. Cheng, Z. Zhang, and P. Heil (2010), Annual cycle of landfast sea ice in Prydz Bay, East Antarctica, *J. Geophys. Res.*, *115*, C02006, doi:10.1029/2008JC005223.

Lei, R., N. Li, P. Heil, B. Cheng, Z. Zhang, and B. Sun (2014), Multiyear sea ice thermal regimes and oceanic heat flux derived from an ice mass balance buoy in the Arctic Ocean, *J. Geophys. Res. Oceans*, *119*, 537–547, doi:10.1002/2012JC008731.

Leppäranta, M., and T. Manninen (1988), The brine and gas content of sea ice with attention to low salinities and high temperatures, technical report 1988-2, *Finn. Inst. of Mar. Res.*, Helsinki, Finland.

Lewis, E. L., and R. G. Perkin (1986), Ice pumps and their rates, *J. Geophys. Res.*, *91*(C10), 11,756–11,762, doi:10.1029/JC091iC10p11756.

- Li, X., D. M. Holland, E. P. Gerber, and C. Yoo (2014), Impacts of the north and tropical Atlantic Ocean on the Antarctic Peninsula and sea ice, *Nature*, *505*(7484), 538–542, doi:10.1038/nature12945.
- Liu, J. P., and J. A. Curry (2010), Accelerated warming of the Southern Ocean and its impacts on the hydrological cycle and sea ice, *Proc. Natl. Acad. Sci. U. S. A.*, *107*(34), 14,987–14,992, doi:10.1073/pnas.1003336107.
- Liu, J. P., J. A. Curry, and D. G. Martinson (2004), Interpretation of recent Antarctic sea ice variability, *Geophys. Res. Lett.*, *31*, L02205, doi:10.1029/2003GL018732.
- Mager, S. M., I. J. Smith, E. W. Kempema, B. J. Thomson, and G. H. Leonard (2013), Anchor ice in polar oceans, *Prog. Phys. Geogr.*, *37*(4), 468–483, doi:10.1177/0309133313479815.
- Mahoney, A. R., A. J. Gough, P. J. Langhorne, N. J. Robinson, C. L. Stevens, M. M. J. Williams, and T. G. Haskell (2011), The seasonal appearance of ice shelf water in coastal Antarctica and its effect on sea ice growth, *J. Geophys. Res.*, *116*, C11032, doi:10.1029/2011JC007060.
- Massom, R. A., K. L. Hill, V. I. Lytle, A. P. Worby, M. Paget, and I. Allison (2001), Effects of regional fast-ice and iceberg distributions on the behaviour of the Mertz Glacier polynya, East Antarctica, *Ann. Glaciol.*, *33*, 391–398, doi:10.3189/172756401781818518.
- McDougall, T., and P. Barker (2011), Getting started with TEOS-10 and the Gibbs Seawater (GSW) Oceanographic Toolbox, 28 pp., SCOR/IAPSO WG127.
- McPhee, M., and N. Untersteiner (1982), Using sea ice to measure vertical heat flux in the ocean, *J. Geophys. Res.*, *87*(C3), 2071–2074, doi:10.1029/JC087iC03p02071.
- Nicolaus, M., C. Katlein, J. Maslanik, and S. Hendricks (2012), Changes in Arctic sea ice result in increasing light transmittance and absorption, *Geophys. Res. Lett.*, *39*, L24501, doi:10.1029/2012GL053738.
- Ohshima, K. I., T. Kawamura, T. Takizawa, S. Ushio, and T. Miyakawa (2000), Current variability under landfast sea ice in Lützow-Holm Bay, Antarctica, *J. Geophys. Res.*, *105*(C7), 17,121–17,132, doi:10.1029/2000JC900080.
- Parkinson, C. L., and D. J. Cavalieri (2012), Antarctic sea ice variability and trends, 1979–2010, *Cryosphere*, *6*, 871–880, doi:10.5194/tc-6-871-2012.
- Paul, S., S. Willmes, M. Hoppmann, P. A. Hunkeler, G. Heinemann, M. Nicolaus, and R. Timmermann (2015), The impact of early summer snow properties on land-fast sea-ice X-band backscatter, *Ann. Glaciol.*, *56*(69), 263–273, doi:10.3189/2015AoG69A715, in press.
- Perovich, D. K., and B. C. Elder (2001), Temporal evolution of Arctic sea-ice temperature, *Ann. Glaciol.*, *33*(1), 207–211.
- Perovich, D. K., S. V. Nghiem, T. Markus, and A. Schweiger (2007), Seasonal evolution and interannual variability of the local solar energy absorbed by the Arctic sea iceocean system, *J. Geophys. Res.*, *112*, C03005, doi:10.1029/2006JC003558.
- Perry, A. (1982), *Hot-Wire Anemometry*, Clarendon, Oxford, U. K.
- Petrich, C., P. Langhorne, and Z. Sun (2006), Modelling the interrelationships between permeability, effective porosity and total porosity in sea ice, *Cold Reg. Sci. Technol.*, *44*(2), 131–144, doi:10.1016/j.coldregions.2005.10.001.
- Pringle, D. J., H. Eicken, H. J. Trodahl, and L. G. E. Backstrom (2007), Thermal conductivity of landfast Antarctic and Arctic sea ice, *J. Geophys. Res.*, *112*, C04017, doi:10.1029/2006JC003641.
- Purdie, C., P. J. Langhorne, G. Leonard, and T. Haskell (2006), Growth of first-year landfast Antarctic sea ice determined from winter temperature measurements, *Ann. Glaciol.*, *44*(1), 170–176, doi:10.3189/1727564067818181853.
- Riche, F., and M. Schneebeli (2013), Thermal conductivity of snow measured by three independent methods and anisotropy considerations, *Cryosphere*, *7*(1), 217–227, doi:10.5194/tc-7-217-2013.
- Richter-Menge, J., D. K. Perovich, B. C. Elder, K. Claffey, I. Rigor, and M. Ortmeier (2006), Ice mass-balance buoys: A tool for measuring and attributing changes in the thickness of the Arctic sea-ice cover, *Ann. Glaciol.*, *44*, 205–210, doi:10.3189/172756406781811727.
- Robinson, N. J., M. J. M. Williams, C. L. Stevens, P. J. Langhorne, and T. G. Haskell (2014), Evolution of a supercooled Ice Shelf Water plume with an actively growing sub-ice platelet matrix, *J. Geophys. Res. Oceans*, *119*, 3425–3446, doi:10.1002/2013JC009399.
- Semtner, A. J. (1976), A model for the thermodynamic growth of sea ice in numerical investigations of climate, *J. Phys. Oceanogr.*, *6*(3), 379–389, doi:10.1175/1520-0485(1976)006<0379:AMFTTG>2.0.CO;2.
- Simpkins, G. R., L. M. Ciasto, D. W. J. Thompson, and M. H. England (2012), Seasonal relationships between large-scale climate variability and Antarctic sea ice concentration, *J. Clim.*, *25*(16), 5451–5469, doi:10.1175/JCLI-D-11-00367.1.
- Smith, I. J., P. J. Langhorne, T. G. Haskell, H. J. Trodahl, R. Frew, and M. R. Vennell (2001), Platelet ice and the land-fast sea ice of McMurdo Sound, Antarctica, *Ann. Glaciol.*, *33*(1), 21–27, doi:10.3189/172756401781818365.
- Smith, I. J., P. J. Langhorne, R. D. Frew, R. Vennell, and T. G. Haskell (2012), Sea ice growth rates near ice shelves, *Cold Reg. Sci. Technol.*, *8384*, 57–70, doi:10.1016/j.coldregions.2012.06.005.
- Stammerjohn, S. E., D. G. Martinson, R. C. Smith, X. Yuan, and D. Rind (2008), Trends in Antarctic annual sea ice retreat and advance and their relation to El Niño Southern Oscillation and Southern Annular Mode variability, *J. Geophys. Res.*, *113*, C03590, doi:10.1029/2007JC004269.
- Sturm, M., and J. B. Johnson (1992), Thermal-conductivity measurements of depth hoar, *J. Geophys. Res.*, *97*(B2), 2129–2139, doi:10.1029/91JB02685.
- Swart, N. C., and J. C. Fyfe (2013), The influence of recent Antarctic ice sheet retreat on simulated sea ice area trends, *Geophys. Res. Lett.*, *40*, 4328–4332, doi:10.1002/grl.50820.
- Swingedouw, D., T. Fichefet, P. Huybrechts, H. Goosse, E. Driesschaert, and M. F. Loutre (2008), Antarctic ice-sheet melting provides negative feedbacks on future climate warming, *Geophys. Res. Lett.*, *35*, L17705, doi:10.1029/2008GL034410.
- Tang, S. L., D. H. Qin, J. W. Ren, J. C. Kang, and Z. J. Li (2007), Structure, salinity and isotopic composition of multi-year landfast sea ice in Nella Fjord, Antarctica, *Cold Reg. Sci. Technol.*, *49*(2), 170–177, doi:10.1016/j.coldregions.2007.03.005.
- Timco, G. W., and R. M. W. Frederking (1996), A review of sea ice density, *Cold Reg. Sci. Technol.*, *24*(1), 1–6, doi:10.1016/0165-232X(95)00007-X.
- Tison, J. L., R. D. Lorrain, A. Bouzette, M. Dini, A. Bondesan, and M. Stiévenard (2013), Linking landfast sea ice variability to marine ice accretion at Hells Gate Ice Shelf, Ross Sea, in *Antarctic Sea Ice: Physical Processes, Interactions and Variability*, edited by M. O. Jeffries, AGU, Washington, D. C., doi:10.1029/AR074p0375.
- Untersteiner, N. (1961), On the mass and heat budget of Arctic sea ice, *Arch. Meteorol. Geophys. Bioklimatol., Ser. A*, *12*(2), 151–182, doi:10.1007/BF02247491.
- Uto, S., H. Shimoda, and S. Ushio (2006), Characteristics of sea-ice thickness and snow-depth distributions of the summer landfast ice in Lützow-Holm Bay, East Antarctica, *Ann. Glaciol.*, *44*(1), 281–287, doi:10.3189/17275640678181240.
- Vacchi, M., M. Mesa, and S. Greco (2000), The Coastal Fish Fauna of Terra Nova Bay, Ross Sea, Antarctica, in *Ross Sea Ecology*, edited by F. M. Faranda, L. Guglielmo, and A. Ianora, chap. 32, pp. 457–468, Springer, Berlin, doi:10.1007/978-3-642-59607-0\_32.
- Vacchi, M., M. La Mesa, M. Dalu, and J. Macdonald (2004), Early life stages in the life cycle of Antarctic silverfish, *Pleuragramma antarcticum* in Terra Nova Bay, Ross Sea, *Antarct. Sci.*, *16*(3), 299–305, doi:10.1017/S0954102004002135.

- Welschmeyer, N. A. (1994), Fluorometric analysis of chlorophyll-a in the presence of chlorophyll-b and pheopigments, *Limnol. Oceanogr.*, 39(8), 1985–1992, doi:10.4319/lo.1994.39.8.1985.
- Yen, Y.-C. (1981), Review of thermal properties of snow, ice and sea ice, technical report, U.S. Army Cold Reg. Res. and Eng. Lab., 81(10), CRREL Report, 35 pp., Hanover, N. H.
- Yen, Y.-C., K. C. Chen, and S. Fukusako (1991), Review of intrinsic thermophysical properties of snow, ice, sea ice, and frost, in *Proceedings of 3rd International Symposium on Cold Regions Heat Transfer, Fairbanks, AK*, June 11–14, edited by J. P. Zarling and S. L. Fausett, pp. 187–218, Univ. of Alaska, Fairbanks.
- Zhang, J. (2007), Increasing Antarctic sea ice under warming atmospheric and oceanic conditions, *J. Clim.*, 20(11), 2515–2529, doi:10.1175/JCLI4136.1.
- Zitterbart, D. P., et al. (2014), Are environmental factors responsible for changed breeding behaviour in emperor penguins?, *Antarct. Sci., FirstView*, 26(5), 563–564, doi:10.1017/S0954102014000285.